

**The Quadratic Magnetic Gradient and Complete Geometry of
Magnetic Field Lines Deduced from Multiple Spacecraft
Measurements**

Chao Shen¹, Chi Zhang^{2,3}, Zhaojin Rong^{2,3}, Zuyin Pu⁴, M. Dunlop^{5,6}, C. Philippe

Escoubet⁷, C. T. Russell⁸, Gang Zeng⁹, Nian Ren¹, J. L. Burch¹⁰, Yufei Zhou¹

¹School of Science, Harbin Institute of Technology, Shenzhen, 518055, China

²Institute of Geology and Geophysics, Chinese Academy of Sciences, Beijing 100029,
China

³College of Earth Science, University of Chinese Academy of Sciences, Beijing, China

⁴School of Earth and Space Sciences, Peking University, Beijing, China

⁵School of Space and Environment, Beihang University, Beijing, China

⁶Rutherford Appleton Laboratory, Chilton, DIDCOT, Oxfordshire OX11 0QX, United
Kingdom

⁷ESA/ESTEC (SCI-SC), Postbus 299, Keplerlaan, 1, 2200 AG Noordwijk, The
Netherlands

⁸University of California, Los Angeles, 603 Charles Young Drive, Los Angeles, CA
90095-1567, USA

⁹School of Mathematics and Physics, Jingchu University of Technology, Jingmen,
China

¹⁰Southwest Research Institute, San Antonio, TX, USA

23 Corresponding author: Chao Shen (shenchao@hit.edu.cn)

24

25 **Key Points:**

26 An explicit algorithm for the quadratic magnetic gradient based on multi-point

27 measurements with iterations is presented for the first time

28

29 The algorithm is applicable for both steady and unsteady structures, and the obtained

30 linear magnetic gradient has second order accuracy

31

32 The complete geometry of the magnetic field lines has been obtained, for the first

33 time, based on multi-point measurements

34

35

36 **Key Words:**

37 Multiple Spacecraft Measurements, Iteration, Quadratic Magnetic Gradient,

38 Geometry of Magnetic Field Lines, Curvature, Torsion, Current Density, Magnetic

39 Flux Ropes

40

41

42

43

44

45 **Abstract**

46

47 Topological configurations of the magnetic field play key roles in the evolution of
48 space plasmas. This paper presents a novel algorithm that can estimate the quadratic
49 magnetic gradient as well as the complete geometrical features of magnetic field lines,
50 based on magnetic field and current density measurements by a multiple spacecraft
51 constellation at 4 or more points. The explicit estimators for the linear and quadratic
52 gradients, the apparent velocity of the magnetic structure and the curvature and
53 torsion of the magnetic field lines can be obtained with well predicted accuracies. The
54 feasibility and accuracy of the method have been verified with thorough tests. The
55 algorithm has been successfully applied to exhibit the geometrical structure of a flux
56 rope. This algorithm has wide applications for uncovering a variety of magnetic
57 configurations in space plasmas.

58

59

60

61

62

63

64

65

Plain Language Summary

The magnetic field plays a key role in the dynamical evolution of space plasmas; it traps and stores plasma particles, and controls the transfer, conversion and release of the energies. The Magnetic field can form various structures, where the magnetic field lines can be bending and twisting. At the present time full imaging of the magnetic field has not been achieved. Therefore, it is very important to estimate the magnetic gradients at every order, as well as the geometrical features (curvature and torsion) of the magnetic field lines (MFLs), from the in situ observations. Although we have successfully deduced the first order magnetic gradient and the curvature from multiple S/C magnetic measurements, it is still not solved how to estimate the high order magnetic gradients and the torsion of MFLs. The research reported here has, for the first time, put forward a novel explicit algorithm, which can acquire the quadratic magnetic gradient and the torsion of MFLs with the 4-point magnetic field and current density measurements as the input. This algorithm has stable accuracies and can be applied effectively to analyze the observations of MMS. This method can find a plenty of applications in space exploration and research.

88

89 **1. Introduction**

90

91 A magnetic field can trap plasma populations; control the transfer, conversion
92 and release of energy in planetary magnetospheres; play a key role in the spatial
93 distribution of the plasmas and development of instabilities, as well as controlling the
94 evolution of substorms and storms. The measurement of the magnetic field in space
95 has been carried out by a limited number of sometime collocated spacecraft placed in
96 various locations. It is therefore important and possible to establish the continuous
97 distribution of the magnetic field, based on multi-point magnetic observations. With
98 two point measurements the gradient of the magnetic field along the spacecraft (S/C)
99 separation line can be obtained; With three point magnetic measurements, the
100 magnetic gradient within the S/C constellation plane can be yielded; while with four
101 or more point magnetic measurements, the three dimensional linear magnetic gradient
102 can be estimated (McComas et al., 1986; Harvey, 1998; Chanteur, 1998; Vogt et al.,
103 2008; Shen et al., 2012a, b; Dunlop et al., 2015; Dunlop et al., 2016; Dunlop et al.,
104 2018; Dunlop et al., 2020). In order to get the quadratic magnetic gradient, 10 S/C
105 magnetic measurements are needed (Chanteur, 1998).

106 In the past, magnetic measurements have been performed with two S/C
107 (ISEE-1/2, DSP, RBSP, ARTEMIS, etc.) [Ogilvie et al., 1977; Liu et al., 2005; Shen et
108 al., 2005; Angelopoulos, 2008], three S/C constellations (THEMIS, Swarm)
109 [Angelopoulos, 2008; Friis-Christensen et al., 2006], and four S/C constellations

(Cluster and MMS) [Escoubet et al., 2001; Balogh et al., 2001; Burch et al., 2016; Russell et al., 2016]. However, presently 10 S/C magnetic field observations in space are on the drawing boards. Deducing the various orders of magnetic gradients fully with a limited number of S/C observations remains an important question.

Attempts to partially solve this problem, have used physical constraints to assist the complete determination of the magnetic gradients [Vogt et al., 2009]. The symmetries in plasma structures and the electromagnetic field laws can also be useful. It has been found by Shen et al., [2012a] that, for a force-free magnetic structure in which the current is field-aligned, the 3 dimensional (3-D) magnetic gradient can be completely obtained with 3 spacecraft magnetic measurements. In their derivation, Ampere's law $\nabla \times \mathbf{B} = \mu_0 \mathbf{j}$ and the solenoidal condition of the magnetic field $\nabla \cdot \mathbf{B} = 0$ are used to reduce the equations. Furthermore, if the force-free magnetic structure is steady and moving with a known relative velocity, only two S/C magnetic observations are needed to gain the complete 9 components of the linear magnetic gradient [Shen et al., 2012b]. Liu et al. (2019) have suggested a method to get the nonlinear distribution of the magnetic field in a stable plasma structure by fitting the second-order Taylor expansion based on 4 S/C magnetic measurements and one S/C current density observations. Torbert et al. (2020) have successfully obtained the 3 D distribution of the magnetic field by using the 4 point magnetic and particle/current density measurements of MMS. In their exploration, they have applied a fitting method to the magnetic field to the third order in magnetic gradient, named the

“25-parameter fit”. However, there still exists no explicit solution to the determination of the quadratic magnetic gradient based on multiple spacecraft measurements.

With multiple S/C magnetic observations, geometrical features of the magnetic field lines can be obtained [Shen et al., 2003, 2008a, b, 2011, 2014; Rong et al., 2011; Lavraud et al., 2016; Xiao et al., 2018]. The geometry of the magnetic field lines (MFLs) so obtained includes the tangential direction (just the direction of the magnetic vector), principal direction (along the curvature vector), binormal vector (the normal of the osculation plane of one MFL), curvature and torsion. However, the torsion of the MFLs has not been obtained in these previous methods. The reason for this is that the torsion of the MFLs depends on the quadratic magnetic gradient, which needs 10 point S/C magnetic measurements [Chanteur, 1998] to be deduced. Therefore, it is necessary to explore the calculation of the torsion of MFLs based on observations of a limited number of S/C, in order to learn this more complete of MFLs in space.

This problem is addressed herein, where an explicit algorithm has been derived to estimate the quadratic magnetic gradient as well as the complete geometrical parameters of the MFLs based on measurements with a limited number of spacecraft. This approach has a wide range of applications for analyzing the magnetic structure in space plasmas.

2. The estimators for the linear and quadratic gradients of magnetic field

It is very important to obtain the quadratic gradient of the magnetic field. With it, we can grasp more accurately the structure of the magnetic field and, uncover the complete geometrical structure of the MFLs, including the Frenet coordinates and curvature, as well as the torsion. In this section, we obtain the explicit estimator of the quadratic magnetic gradient based on magnetic field and current density measurements from a multi-S/C constellation.

We present the derivations of this algorithm as follows.

The configuration of the four-spacecraft constellation (Cluster or MMS) is illustrated in Figure 1.

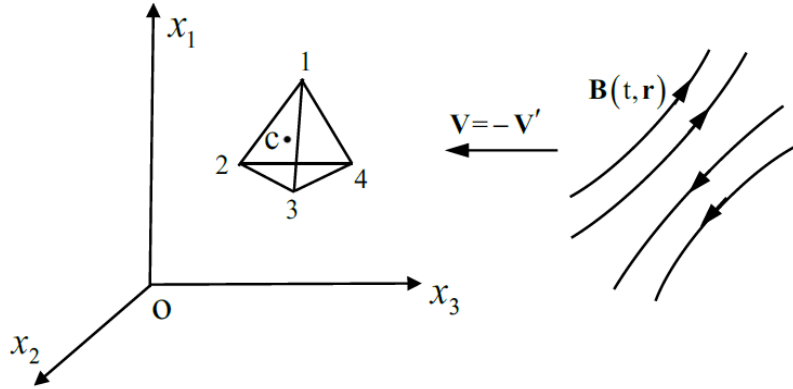


Figure 1. The exploration on the magnetic field in space in the S/C constellation frame of reference. (x_1, x_2, x_3) are the Cartesian coordinates in the S/C constellation reference frame. The S/C constellation is composed of four spacecraft (the number of spacecraft can be more 4), whose barycenter is at the point C. The apparent motional velocity of the magnetic field structure relative to the S/C constellation reference is

\mathbf{V} . Conversely, the velocity of the S/C constellation relative to the proper reference of the magnetic field structure is $\mathbf{V}' = -\mathbf{V}$.

In the S/C constellation frame of reference, the simultaneous position vectors of the four spacecraft are \mathbf{r}_α ($\alpha=1,2,3,4$) and the position vector of the barycenter of the four S/C is

$$\mathbf{r}_c = \frac{1}{4} \sum_{\alpha=1}^4 \mathbf{r}_\alpha . \quad (1)$$

In this study, the Greek subscripts or superscripts apply to spacecraft, and $\alpha, \beta, \gamma, \dots=1, 2, 3, 4$; while the Latin subscript c indicates the barycenter.

The apparent motional velocity of the magnetic field structure relative to the S/C constellation reference frame is denoted as \mathbf{V} , which may vary from point to point [Hamrin, et al.(2008)]. The velocity of the S/C constellation relative to the proper reference frame of the magnetic field structure is $\mathbf{V}' = -\mathbf{V}$. We establish the Cartesian coordinates (x_1, x_2, x_3) in the S/C constellation reference, and choose the x_3 axis along the direction of $\mathbf{V}' = -\mathbf{V}$ with its basis $\hat{\mathbf{x}}_3 = -\mathbf{V} / V$. The configuration of the S/C constellation is characterized by the volume tensor, which is defined [Harvey, 1998; Shen et al., 2003] as

$$\mathbf{R}_{kj} = \frac{1}{4} \sum_{\alpha=1}^4 (\mathbf{r}_{\alpha k} - \mathbf{r}_{ck}) (\mathbf{r}_{\alpha j} - \mathbf{r}_{cj}) . \quad (2)$$

We have applied some Latin subscripts or superscripts (other than c) to denote Cartesian coordinates with i, j, k, e, m, n=1, 2, 3 and p, q, s, r=1, 2 .

(i) The linear gradients of the magnetic field and current density at the barycenter

As the MMS S/C cross a magnetic structure, the four S/C measure the magnetic field with high accuracy and time resolution [Russell et al. 2014; Burch et al. 2015].

The magnetic field observed by the α th S/C at position \mathbf{r}_α is

$$\mathbf{B}_\alpha(t) = \mathbf{B}(t, \mathbf{r}_\alpha), \alpha = 1, 2, 3, 4. \quad (3)$$

The MMS S/C can measure the distributions of ions and electrons with an efficient accuracy to yield the local current density [Torbert et al., 2015, 2020] as

$$\mathbf{j}_\alpha(t) = \mathbf{j}(t, \mathbf{r}_\alpha), \alpha = 1, 2, 3, 4. \quad (4)$$

To obtain the magnetic field and its first order gradient at the barycenter of the MMS constellation, we first neglect the second order magnetic gradient under the linear approximation. With four S/C, simultaneous magnetic observations, the magnetic field and its linear gradient at the barycenter of the S/C constellation can be obtained with the previous methods established by Harvey (1998) and Chanteur (1998). In order to suppress the fluctuating components in the magnetic field and obtain the magnetic gradient at higher accuracy, we make use of the time series of the magnetic observations by the four S/C to get the magnetic gradient with the method first put forward by De Keyser, et al. (2007). In their approach, the time series data of the four S/C do not need to be synchronized. Appendix A gives the explicit estimator of the linear gradient of magnetic field in space and time from this approach.

Based on equations (A14) and (A15) in Appendix A, the magnetic field and its first order derivatives at the barycenter of the MMS constellation under the linear approximation are as follows.

$$B_i(t_c, \mathbf{r}_c) = \frac{1}{4n} \sum_{a=1}^{4n} B_i(t_a, \mathbf{r}_a), \quad (5)$$

$$\nabla_\nu B_i(t_c, \mathbf{r}_c) = R_{\nu\mu}^{-1} \cdot \frac{1}{4n} \sum_{a=1}^{4n} (x_{(a)}^\mu - x_0^\mu) B_i(t_a, \mathbf{r}_a). \quad (6)$$

And the above formulas in the vector format are

$$\mathbf{B}(t_c, \mathbf{r}_c) = \frac{1}{4n} \sum_{a=1}^{4n} \mathbf{B}(t_a, \mathbf{r}_a), \quad (7)$$

$$\nabla_\nu \mathbf{B}(t_c, \mathbf{r}_c) = R_{\nu\mu}^{-1} \cdot \frac{1}{4n} \sum_{a=1}^{4n} (x_{(a)}^\mu - x_0^\mu) \mathbf{B}(t_a, \mathbf{r}_a). \quad (8)$$

In the above formulas (5)-(8), the general volume tensor $R^{\mu\nu}$ in spacetime is defined by (A9). These equations will yield the time series of magnetic field $\mathbf{B}(t_c, \mathbf{r}_c)$, its time derivative $\partial_t \mathbf{B}(t_c, \mathbf{r}_c)$ and first order gradient $\nabla \mathbf{B}(t_c, \mathbf{r}_c)$ at the barycenter of the S/C constellation.

In the above formulas (5)-(8), the accuracy is found to first order due to omission of the second order gradients. We will correct the magnetic field and its first order derivatives at the barycenter with the second order derivatives of the magnetic field according to Appendix A and will further obtain the corrected quadratic magnetic gradient by iteration (see (vii) later). The corrected magnetic field and its first order gradient at the barycenter will then have second order accuracy.

In this investigation, we have neglected the magnetic gradients with orders higher than two, so that the current density can be regarded as linearly varying.

According to the Equations (A14) and (A15) in Appendix A, the current density at the barycenter is

$$\mathbf{j}_c = \mathbf{j}(t_c, \mathbf{r}_c) = \frac{1}{4n} \sum_{a=1}^{4n} \mathbf{j}(t_a, \mathbf{r}_a), \quad (9)$$

and the linear gradient of the current density at the barycenter is

$$\nabla_\nu \mathbf{j}(t_c, \mathbf{r}_c) = \mathbf{R}_{\nu\mu}^{-1} \cdot \frac{1}{4n} \sum_{a=1}^{4n} (x_{(a)}^\mu - x_0^\mu) \mathbf{j}(t_a, \mathbf{r}_a), \quad (10)$$

of which the component form is

$$\nabla_\nu j_k(t_c, \mathbf{r}_c) = \mathbf{R}_{\nu\mu}^{-1} \cdot \frac{1}{4n} \sum_{a=1}^{4n} (x_{(a)}^\mu - x_0^\mu) j_k(t_a, \mathbf{r}_a). \quad (10')$$

Generally, the electron and ion measurements have different time resolutions. So that the electron and ion current densities and their linear gradients at the barycenter can be first calculated separately with Equations (9) and (10), and finally added to obtain the total current density and its linear gradient at the barycenter.

(ii) The second order time derivative of the magnetic field and the first order time derivative of the magnetic gradient

With the time series of magnetic field $\mathbf{B}(t_c, \mathbf{r}_c)$ and its first order time derivative $\partial_t \mathbf{B}(t_c, \mathbf{r}_c)$ at the barycenter obtained in (i), it is easy to get the second order time derivative of magnetic field $\partial_t \partial_t \mathbf{B}(t_c, \mathbf{r}_c)$ at the barycenter, where $\partial_t \equiv \partial/\partial t$.

The gradient of the time derivative of the magnetic field is equivalent to the time derivative of the magnetic gradient, i.e.,

$$\nabla_j \partial_t B_i(t, \mathbf{r}) = \partial_t [\nabla_j B_i(t, \mathbf{r})]. \quad (11)$$

Therefore, at the central point (t_c, \mathbf{r}_c) ,

$$\nabla_j \partial_t B_i(t_c, \mathbf{r}_c) = \partial_t \nabla_j B_i(t_c, \mathbf{r}_c) = \frac{\partial}{\partial t_c} [\nabla_j B_i(t_c, \mathbf{r}_c)]. \quad (12)$$

253

254 **(iii) The transformations between the temporal and spatial gradients of the**
 255 **magnetic field in different reference frames**

256 This approach will make use of the proper reference frame of the magnetic
 257 structure so as to determine the second order gradient in the direction of the apparent
 258 motion of the magnetic structure, i.e., the longitudinal quadratic gradient of the
 259 magnetic field. To do this, we need to find the apparent velocity \mathbf{V} of the magnetic
 260 structure relative to the spacecraft constellation. For space plasmas, this relative
 261 velocity is much less than the speed of the light in vacuum, i.e., $V \ll c$. Shi et al.
 262 (2006) have first obtained the velocity of the magnetic structure relative to the
 263 spacecraft with the temporal and spatial variation rates of the magnetic field under
 264 the assumption of stationarity. Hamrin et al. (2008) have obtained the apparent
 265 velocity of the magnetic structure using a proper reference frame. Here we give a
 266 concise discussion on the transformations between the temporal and spatial gradients
 267 of the magnetic field in different reference frames.

268 The time and space coordinates (t, \mathbf{r}) in the S/C constellation reference frame
 269 and the corresponding time and space coordinates (t', \mathbf{r}') in the proper reference
 270 frame of the magnetic structure obey the Galilean transformations, i.e., $t' = t$,
 271 $\mathbf{r}' = \mathbf{r} - \mathbf{V}t$ (see also Figure 1). (The Eulerian description is applied in each reference
 272 frame.) The magnetic fields observed in the S/C constellation frame and the proper
 273 frame of the magnetic structure are $\mathbf{B}(t, \mathbf{r})$ and $\mathbf{B}'(t', \mathbf{r}')$, respectively. As $V \ll c$,

$\mathbf{B}(\mathbf{t}, \mathbf{r}) = \mathbf{B}'(\mathbf{t}', \mathbf{r}')$. It is obvious that the magnetic gradient in these two reference frames are also identical, i.e.,

$$\nabla \mathbf{B}(\mathbf{t}, \mathbf{r}) = \nabla' \mathbf{B}'(\mathbf{t}', \mathbf{r}'). \quad (13)$$

The relationship between the time derivative of the magnetic field in the S/C constellation, $\frac{\partial \mathbf{B}(\mathbf{t}, \mathbf{r})}{\partial t}$, and time derivative of the magnetic field in the proper

reference frame of the magnetic structure, $\frac{\partial \mathbf{B}'(\mathbf{t}', \mathbf{r}')}{\partial t'}$, is

$$\frac{\partial \mathbf{B}(\mathbf{t}, \mathbf{r})}{\partial t} = \frac{\partial \mathbf{B}'(\mathbf{t}', \mathbf{r}')}{\partial t} = \frac{\partial t'}{\partial t} \frac{\partial \mathbf{B}'(\mathbf{t}', \mathbf{r}')}{\partial t'} + \frac{\partial \mathbf{r}'}{\partial t} \cdot \nabla' \mathbf{B}'(\mathbf{t}', \mathbf{r}'),$$

or

$$\frac{\partial \mathbf{B}(\mathbf{t}, \mathbf{r})}{\partial t} = \frac{\partial \mathbf{B}'(\mathbf{t}', \mathbf{r}')}{\partial t'} - \mathbf{V} \cdot \nabla \mathbf{B}(\mathbf{t}, \mathbf{r}). \quad (14)$$

Which is the same formula as given by Song and Russell (1999) and Shi et al. (2006).

In the proper reference frame of the magnetic structure, $\frac{\partial \mathbf{B}'(\mathbf{t}', \mathbf{r}')}{\partial t'} = 0$, thus

$$\frac{\partial \mathbf{B}(\mathbf{t}, \mathbf{r})}{\partial t} = -\mathbf{V}(\mathbf{t}, \mathbf{r}) \cdot \nabla \mathbf{B}(\mathbf{t}, \mathbf{r}). \quad (15)$$

At the barycenter of the S/C constellation,

$$\frac{\partial \mathbf{B}(\mathbf{t}, \mathbf{r}_c)}{\partial t} = -\mathbf{V}(\mathbf{t}, \mathbf{r}_c) \cdot \nabla \mathbf{B}(\mathbf{t}, \mathbf{r}_c). \quad (16)$$

The component form of the above formula is

$$\frac{\partial B_j(\mathbf{t}, \mathbf{r}_c)}{\partial t} = -V_i(\mathbf{t}, \mathbf{r}_c) \cdot \nabla_i B_j(\mathbf{t}, \mathbf{r}_c). \quad (16')$$

The above equation has a unique solution of the apparent velocity and a proper reference frame can be found only if $|\nabla \mathbf{B}(\mathbf{t}, \mathbf{r})| \neq 0$. Thus the apparent velocity of the magnetic structure relative to the S/C constellation is (Shi et al., 2006; Hamrin et al., 2008)

$$\mathbf{V}_i(\mathbf{t}, \mathbf{r}_c) = -\mathbf{V}'_i(\mathbf{t}, \mathbf{r}_c) = -\partial_t \mathbf{B}_j(\mathbf{t}, \mathbf{r}_c) \cdot (\nabla \mathbf{B})_{ji}^{-1}(\mathbf{t}, \mathbf{r}_c). \quad (17)$$

It is noted that the apparent velocity of the magnetic structure can vary with time. The formula (17) is applicable for magnetic structures with $V \ll c$, whether steady or unsteady. \mathbf{V}/V is a characteristic, directional vector, so that we can define $-\mathbf{V}/V$ as the directional vector of the x_3 axis in the S/C constellation reference frame, i.e., $\hat{\mathbf{x}}_3 = -\mathbf{V}/V$.

We can further investigate the transformation between the time derivatives of the magnetic gradients in the two different reference frames. Similarly to the linear magnetic gradients in the formula (13), the quadratic magnetic gradients in the S/C constellation frame and the proper frame of the magnetic structure are identical, i.e.,

$$\nabla \nabla \mathbf{B}(\mathbf{t}, \mathbf{r}) = \nabla' \nabla' \mathbf{B}'(\mathbf{t}', \mathbf{r}'). \quad (18)$$

The relationship between the time derivative of the magnetic gradient in the S/C constellation frame, $\partial_t \nabla \mathbf{B}(\mathbf{t}, \mathbf{r})$, and the time derivative of the magnetic gradient in the proper frame of the magnetic structure, $\partial_{t'} \nabla' \mathbf{B}'(\mathbf{t}', \mathbf{r}')$, satisfies

$$\begin{aligned} \frac{\partial}{\partial t} \nabla \mathbf{B}(\mathbf{t}, \mathbf{r}) &= \frac{\partial}{\partial t} \nabla' \mathbf{B}'(\mathbf{t}', \mathbf{r}') \\ &= \frac{\partial t'}{\partial t} \frac{\partial}{\partial t'} \nabla' \mathbf{B}'(\mathbf{t}', \mathbf{r}') + \frac{\partial \mathbf{r}'}{\partial t} \cdot \nabla' \nabla' \mathbf{B}'(\mathbf{t}', \mathbf{r}') \\ &= \nabla' \frac{\partial}{\partial t'} \mathbf{B}'(\mathbf{t}', \mathbf{r}') - \mathbf{V} \cdot \nabla' \nabla' \mathbf{B}'(\mathbf{t}', \mathbf{r}'). \end{aligned} \quad (19)$$

Considering $\frac{\partial \mathbf{B}'(\mathbf{t}', \mathbf{r}')}{\partial t'} = 0$ in the proper reference frame and the equation (18), this

reduces to

$$\frac{\partial}{\partial t} \nabla \mathbf{B}(\mathbf{t}, \mathbf{r}) = -\mathbf{V} \cdot \nabla \nabla \mathbf{B}(\mathbf{t}, \mathbf{r}), \quad (20)$$

which is the formula relating the time derivative of the linear magnetic gradient to the quadratic magnetic gradient in the S/C constellation reference frame. With this general formula the gradient of the linear magnetic gradient in the direction of apparent velocity is readily obtained as shown below in (iv).

(iv) The longitudinal gradient of $\nabla \mathbf{B}(\mathbf{t}, \mathbf{r}_c)$

Based on Equation (20), the gradient of the linear magnetic gradient along the x_3 direction at the barycenter \mathbf{r}_c satisfies

$$\mathbf{V} \frac{\partial}{\partial x^3} \nabla \mathbf{B}(\mathbf{t}, \mathbf{r}_c) = \partial_t \nabla \mathbf{B}(\mathbf{t}, \mathbf{r}_c), \quad (21)$$

or

$$\partial_3 \partial_k \mathbf{B}_m(\mathbf{t}, \mathbf{r}_c) = \frac{1}{V} \partial_t \partial_k \mathbf{B}_m(\mathbf{t}, \mathbf{r}_c). \quad (22)$$

The right hand side of the above equation can be obtained from Equation (12), so that 9 components of the quadratic magnetic gradient can be obtained. Formula (22) is applicable for both steady and unsteady magnetic structures.

Furthermore, due to the symmetry of the quadratic gradient,

$$\nabla_p \nabla_3 \mathbf{B}_1 = \nabla_3 \nabla_p \mathbf{B}_1, \quad (23)$$

of which the right hand side is given by Equation (20), so that 6 more components of the quadratic magnetic gradient can be obtained. Now only $\nabla_p \nabla_q \mathbf{B}_l$ ($p, q = 1, 2, l = 1, 2, 3$) are to be found, which involve $4 \times 3 = 12$ components. Considering the symmetry of the quadratic magnetic gradient, $\nabla_p \nabla_q \mathbf{B}_l = \nabla_q \nabla_p \mathbf{B}_l$, only $3 \times 3 = 9$ of these components are independent.

The gradient of the current density will be needed for the estimation of the remaining components of the quadratic magnetic gradient.

(v) Three components and two constraints for the quadratic magnetic gradient using the gradient of current density

From Ampere's law, we get the constraints that

$$\nabla(\nabla \times \mathbf{B}) = \nabla \mathbf{j},$$

with which we can obtain some components of the quadratic magnetic gradient if $\nabla \mathbf{j}$ is known (for simplicity, we replace $\mu_0 \mathbf{j}$ by \mathbf{j}). If the electromagnetic fields are strongly varying, $\mathbf{j} = \nabla \times \mathbf{B} - c^{-2} \partial \mathbf{E} / \partial t$, with the electric displacement current included. However, in this investigation we only consider the slow-varying electromagnetic fields with the limitation $|\nabla \times \mathbf{B}| \gg c^{-2} |\partial \mathbf{E} / \partial t|$, which is commonly satisfied in large scale space plasmas. The component equation $\partial_3 (\nabla \times \mathbf{B}) = \partial_3 \mathbf{j}$ is not an independent constraint due to Eq. (22). It is a surplus condition, which we have not used because Eq. (22) can yield the longitudinal gradient directly already. Furthermore, $\nabla \cdot \mathbf{j} = \nabla \cdot (\nabla \times \mathbf{B}) = 0$, so that the gradient of the current density only provides 9-3-1=5 independent constraints.

The transverse quadratic gradient of the longitudinal magnetic field, i.e., the quadratic gradient of the magnetic component B_3 in the plane orthogonal to the direction of motion (or x_3 direction) satisfies

$$\partial_p \partial_q B_3 = \partial_p (\partial_{[q} B_{3]} + \partial_3 B_q) = \partial_p (\epsilon_{lq3} j_l + \partial_3 B_q), \quad (24)$$

Where again Ampere's law $\nabla \times \mathbf{B} = \mathbf{j}$ has been used. Thus, Equation (24) leads to

$$\partial_p \partial_q B_3(\mathbf{t}, \mathbf{r}_c) = \varepsilon_{lq3} \partial_p j_l(\mathbf{t}, \mathbf{r}_c) + \partial_3 \partial_p B_q(\mathbf{t}, \mathbf{r}_c), \quad (25)$$

where $\partial_p j_q$ is used. The above formula yields the transverse quadratic magnetic gradient of the longitudinal magnetic field and contains 3 independent components of the quadratic magnetic gradient at the barycenter.

There are still 6 components of the quadratic magnetic gradient remaining to be determined, i.e., $\partial_p \partial_q B_s(\mathbf{t}, \mathbf{r}_c)$, which are the transverse quadratic gradients of the transverse magnetic field.

Two additional constraints can be obtained from

$$\partial_p j_3 = \partial_p (\partial_1 B_2 - \partial_2 B_1), \quad (p, q = 1, 2), \text{ i.e.,}$$

$$\begin{cases} \partial_1 \partial_1 B_2 - \partial_1 \partial_2 B_1 = \partial_1 j_3 \\ \partial_2 \partial_1 B_2 - \partial_2 \partial_2 B_1 = \partial_2 j_3 \end{cases} \quad (26)$$

$$\quad \quad \quad \begin{cases} \partial_2 \partial_1 B_2 - \partial_2 \partial_2 B_1 = \partial_2 j_3 \\ \partial_1 \partial_1 B_2 - \partial_1 \partial_2 B_1 = \partial_1 j_3 \end{cases} \quad (27)$$

which is at the barycenter.

Based on Ampere's law, therefore, 3 more components of the quadratic magnetic gradient and 2 constraints on it can be obtained with the gradient of current density as shown in the formulas (25), (26) and (27).

Now 4 constraints are to be found for the complete determination of the quadratic magnetic gradient.

(xi) The last four constraints

The magnetic field is divergence-free, i.e., $\nabla \cdot \mathbf{B} = 0$. Therefore

$$\partial_j \partial_k B_k = 0. \quad (28)$$

It is noted that the sum over k is made in the above formula. Because

$\partial_3 \partial_k B_k = 0$ is a dependent constraint in Equation (22), there are only

two independent constraints, i.e., $\partial_p \partial_k B_k = 0, (p, q = 1, 2)$. So that

$$\partial_1 \partial_1 B_1 + \partial_1 \partial_2 B_2 = -\partial_1 \partial_3 B_3, \quad (29)$$

$$\partial_2 \partial_1 B_1 + \partial_2 \partial_2 B_2 = -\partial_2 \partial_3 B_3, \quad (30)$$

where $\partial_p \partial_3 B_3 = \partial_3 \partial_p B_3 = \frac{1}{V} \partial_p \partial_t B_3$ according to Eq. (22).

There are therefore only two constraints left to be found.

Using magnetic rotation analysis (MRA) [Shen et al., 2007, see also Appendix B], the remaining two constraints can be obtained from the properties of the magnetic field. As shown in Appendix B, based on MRA, the magnetic rotation tensor has three characteristic directions $(\hat{\mathbf{X}}_1, \hat{\mathbf{X}}_2, \hat{\mathbf{X}}_3)$, as illustrated here in Figure 2. The coordinate line X_3 is along $\hat{\mathbf{X}}_3$. In the third characteristic direction $\hat{\mathbf{X}}_3$, the magnetic unit vector $\hat{\mathbf{b}} = \mathbf{B}/B$ has no rotation, and the square of the magnetic rotation rate is

$$\frac{\partial \hat{\mathbf{b}}}{\partial X_3} \cdot \frac{\partial \hat{\mathbf{b}}}{\partial X_3} = 0. \quad (31)$$

So that

$$\frac{\partial \hat{\mathbf{b}}}{\partial X_3} = 0. \quad (32)$$

Since $\frac{\partial \hat{\mathbf{b}}}{\partial X_3} = 0$ at each point of the coordinate line X_3 (as indicated in Figure 2),

we have

$$\frac{\partial}{\partial X_3} \frac{\partial \hat{\mathbf{b}}}{\partial X_3} = 0. \quad (33)$$

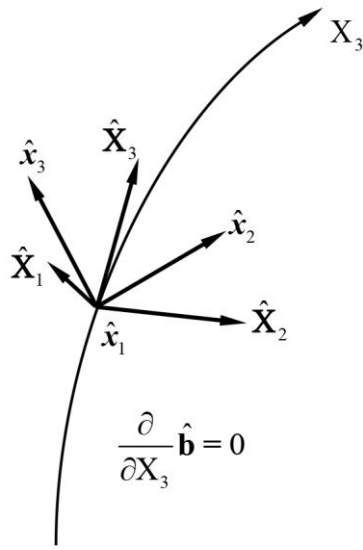


Figure 2. Illustration of the characteristic direction at which the magnetic rotation minimizes.

Since the magnetic unit vector $\hat{\mathbf{b}}$ obeys $\hat{\mathbf{b}} \cdot \hat{\mathbf{b}} = 1$, the above constraint contains only two independent component equations, which can be chosen as

$$\frac{\partial}{\partial X_3} \frac{\partial}{\partial X_3} \frac{B_p}{B} = 0, \quad p=1, 2. \quad (34)$$

The three characteristic directions $(\hat{\mathbf{X}}_1, \hat{\mathbf{X}}_2, \hat{\mathbf{X}}_3)$ have a relationship with the base vectors $(\hat{\mathbf{x}}_1, \hat{\mathbf{x}}_2, \hat{\mathbf{x}}_3)$ of the S/C coordinates (x_1, x_2, x_3) , as follows:

$$\hat{\mathbf{X}}_i = a_{ij} \hat{\mathbf{x}}_j, \quad (35)$$

where the coefficients $a_{ij} = \hat{\mathbf{X}}_i \cdot \hat{\mathbf{x}}_j = \cos \left[\angle (\hat{\mathbf{X}}_i, \hat{\mathbf{x}}_j) \right]$. If we assume a vector

$$\mathbf{X} = x_i \hat{\mathbf{x}}_i = X_j \hat{\mathbf{X}}_j, \quad \text{then} \quad x_i = X_j \hat{\mathbf{X}}_j \cdot \hat{\mathbf{x}}_i = a_{ji} X_j.$$

The first order partial derivative obeys:

$$\frac{\partial}{\partial X_3} = \frac{\partial}{\partial x_k} \cdot \frac{\partial x_k}{\partial X_3} = a_{3k} \frac{\partial}{\partial x_k},$$

and the second order partial derivative obeys:

$$\frac{\partial}{\partial \mathbf{X}_3} \frac{\partial}{\partial \mathbf{X}_3} = a_{3k} \frac{\partial}{\partial x_k} \left(a_{3j} \frac{\partial}{\partial x_j} \right) = a_{3k} a_{3j} \frac{\partial}{\partial x_k} \frac{\partial}{\partial x_j}.$$

Generally, $\hat{\mathbf{X}}_3$ is varying slowly in space and $\frac{\partial}{\partial x_k} a_{3j}$ is a small quantity, thus

$\frac{\partial}{\partial x_k} a_{3j}$ is omitted in the above equations. Therefore, Equation (34) reduces to

$$a_{3k} a_{3j} \frac{\partial}{\partial x^k} \frac{\partial}{\partial x^j} \left(\frac{\mathbf{B}_p}{\mathbf{B}} \right) = 0, \quad p=1, 2. \quad (36)$$

Finally, we show below that we can find $\partial_p \partial_q \mathbf{B}_s(\mathbf{t}, \mathbf{r}_c)$ by combining the equations (26), (27), (29), (30) and (36).

We also can investigate the formula (36) in more detail. For simplicity, we can adjust the coordinates (x_1, x_2, x_3) . We keep the x_3 axis unchanged with its basis $\hat{\mathbf{x}}_3 = -\mathbf{V} / V$, and rotate x_1 and x_2 axes around the x_3 axis such that the coordinate base vector $\hat{\mathbf{x}}_1$ is orthogonal to both $\hat{\mathbf{x}}_3$ and $\hat{\mathbf{X}}_3$, i.e.,

$$\hat{\mathbf{x}}_1 = \frac{\hat{\mathbf{X}}_3 \times \hat{\mathbf{x}}_3}{|\hat{\mathbf{X}}_3 \times \hat{\mathbf{x}}_3|}, \quad (37)$$

(and as illustrated in Figure 2). Thus

$$a_{31} = \hat{\mathbf{X}}_3 \cdot \hat{\mathbf{x}}_1 = 0.$$

Then the formula (36) becomes

$$a_{32}^2 \frac{\partial^2}{\partial x_2^2} \left(\frac{\mathbf{B}_p}{\mathbf{B}} \right) = -a_{33}^2 \frac{\partial^2}{\partial x_3^2} \left(\frac{\mathbf{B}_p}{\mathbf{B}} \right) - 2a_{33} a_{32} \frac{\partial}{\partial x_3} \frac{\partial}{\partial x_2} \left(\frac{\mathbf{B}_p}{\mathbf{B}} \right). \quad (38)$$

All the terms in the right hand side of the above equation are known. With the formula (59) developed in the next section, we can express the second order gradients of the

components of the magnetic unit vector on the two sides of Eq. (38) in terms of the magnetic gradients. With the formula (59), we get

$$\frac{\partial}{\partial x_2} \frac{\partial}{\partial x_2} \left(\frac{\mathbf{B}_p}{\mathbf{B}} \right) = \mathbf{B}^{-1} \partial_2 \partial_2 \mathbf{B}_p - \mathbf{B}^{-3} \mathbf{B}_p \mathbf{B}_1 \partial_2 \partial_2 \mathbf{B}_1 - 2\mathbf{B}^{-2} \partial_2 \mathbf{B}_p \partial_2 \mathbf{B} + 3\mathbf{B}^{-3} \mathbf{B}_p \partial_2 \mathbf{B} \partial_2 \mathbf{B} - \mathbf{B}^{-3} \mathbf{B}_p \partial_2 \mathbf{B}_1 \partial_2 \mathbf{B}_1$$

,

or

$$\partial_2 \partial_2 \left(\frac{\mathbf{B}_p}{\mathbf{B}} \right) = \left(\mathbf{B}^{-1} \partial_2 \partial_2 \mathbf{B}_p - \mathbf{B}^{-3} \mathbf{B}_p \mathbf{B}_s \partial_2 \partial_2 \mathbf{B}_s \right) + \left(-\mathbf{B}^{-3} \mathbf{B}_p \mathbf{B}_3 \partial_2 \partial_2 \mathbf{B}_3 - 2\mathbf{B}^{-2} \partial_2 \mathbf{B}_p \partial_2 \mathbf{B} + 3\mathbf{B}^{-3} \mathbf{B}_p \partial_2 \mathbf{B} \partial_2 \mathbf{B} - \mathbf{B}^{-3} \mathbf{B}_p \partial_2 \mathbf{B}_1 \partial_2 \mathbf{B}_1 \right)$$

The second expression on the right hand side is known already. Substituting (39') into (38), we get

$$\mathbf{B}^{-1} \partial_2 \partial_2 \mathbf{B}_p - \sum_{s=1}^2 \mathbf{B}^{-3} \mathbf{B}_p \mathbf{B}_s \partial_2 \partial_2 \mathbf{B}_s = -\frac{a_{33}^2}{a_{32}^2} \frac{\partial^2}{\partial x_3^2} \left(\frac{\mathbf{B}_p}{\mathbf{B}} \right) - \frac{2a_{33}}{a_{32}} \partial_3 \partial_2 \frac{\mathbf{B}_p}{\mathbf{B}} - \left[-\mathbf{B}^{-3} \mathbf{B}_p \mathbf{B}_3 \partial_2 \partial_2 \mathbf{B}_3 - 2\mathbf{B}^{-2} \partial_2 \mathbf{B}_p \partial_2 \mathbf{B} + 3\mathbf{B}^{-3} \mathbf{B}_p \partial_2 \mathbf{B} \partial_2 \mathbf{B} - \mathbf{B}^{-3} \mathbf{B}_p \partial_2 \mathbf{B}_1 \partial_2 \mathbf{B}_1 \right]$$

where $p=1, 2$. All the terms in the right hand side of the above equation can be determined with (59), (8), (22), (23) and (24).

Therefore, combining equations (26), (27), (29), (30) and (40), we can determine

$$\partial_p \partial_q \mathbf{B}_s (\mathbf{t}, \mathbf{r}_c).$$

Actually, with the two equations in the formula (40), we can completely find the solution $\partial_2 \partial_2 \mathbf{B}_s (\mathbf{t}, \mathbf{r}_c)$, ($s=1, 2$).

Furthermore, with the formulas (30) and (27), we can get $\partial_1 \partial_2 \mathbf{B}_s (\mathbf{t}, \mathbf{r}_c)$, ($s=1, 2$), i.e.,

$$\partial_1 \partial_2 \mathbf{B}_1 = \partial_2 \partial_1 \mathbf{B}_1 = -\partial_2 \partial_2 \mathbf{B}_2 - \partial_2 \partial_3 \mathbf{B}_3,$$

and

$$\partial_1 \partial_2 \mathbf{B}_2 = \partial_2 \partial_1 \mathbf{B}_2 = \partial_2 \partial_2 \mathbf{B}_1 + \partial_2 \mathbf{j}_3. \quad (42)$$

The above two equations are valid at the barycenter.

In addition, from the equation (29) and (26), we can obtain $\partial_1 \partial_1 \mathbf{B}_s(\mathbf{t}, \mathbf{r}_c)$, ($s=1, 2$), i.e.,

$$\partial_1 \partial_1 \mathbf{B}_1 = -\partial_1 \partial_2 \mathbf{B}_2 - \partial_1 \partial_3 \mathbf{B}_3, \quad (43)$$

and

$$\partial_1 \partial_1 \mathbf{B}_2 = \partial_1 \partial_2 \mathbf{B}_1 + \partial_1 \mathbf{j}_3. \quad (44)$$

The above two equations are also valid at the barycenter.

So far, we have obtained all the components of the quadratic gradient $(\nabla \nabla \mathbf{B})_c$ at the barycenter. The accuracy of the quadratic gradient is to first order, just as that for the magnetic gradient.

(vii) Recalculating the magnetic gradients by iteration

In order to enhance the accuracy of the magnetic quantities, we can correct the estimate of the field and its linear gradient at the barycenter with the quadratic magnetic gradient obtained above (based on the formulae (A8) and (A13) in Appendix A). Subsequently, we can further go through the above steps (ii) - (vi) to get the corrected quadratic magnetic gradient with better accuracy.

The procedure is as follows:

The magnetic field measured by the four spacecraft is

$$B_i(t_a, \mathbf{r}_a) = B_i(t_c, \mathbf{r}_c) + \Delta x_a^\nu \nabla_\nu B_i(t_c, \mathbf{r}_c) + \frac{1}{2} \Delta x_a^\nu \Delta x_a^\lambda \nabla_\nu \nabla_\lambda B_i(t_c, \mathbf{r}_c). \quad (45)$$

Based on the formula (A8) in Appendix A, we obtain the magnetic field at the barycenter, corrected by the quadratic magnetic gradient, as:

$$\mathbf{B}_i(\mathbf{t}_c, \mathbf{r}_c) = \frac{1}{4n} \sum_{a=1}^{4n} \mathbf{B}_i(\mathbf{t}_a, \mathbf{r}_a) - \frac{1}{2} \mathbf{R}^{\nu\lambda} \nabla_\nu \nabla_\lambda \mathbf{B}_i(\mathbf{t}_c, \mathbf{r}_c), \quad (46)$$

where, the general volume tensor $\mathbf{R}^{\nu\lambda}$ is as defined in (A9).

From the formula (A13) in Appendix A, we get the first order magnetic gradient at the barycenter corrected from the quadratic magnetic gradient as

$$\nabla_\nu \mathbf{B}_i(\mathbf{t}_c, \mathbf{r}_c) = \left(\mathbf{R}^{-1} \right)_{\nu\mu} \cdot \frac{1}{N} \sum_a^N \left(x_{(a)}^\mu - x_c^\mu \right) \mathbf{B}_i(\mathbf{t}_a, \mathbf{r}_a) - \frac{1}{2} \left(\mathbf{R}^{-1} \right)_{\nu\mu} \mathbf{R}^{\mu\sigma\lambda} \nabla_\sigma \nabla_\lambda \mathbf{B}_i(\mathbf{t}_c, \mathbf{r}_c).$$

(47)

Furthermore, we can perform the above steps (ii) - (vi) to obtain the corrected quadratic magnetic gradient using these updated estimates. The quadratic magnetic gradient obtained in this iterative sense has a higher accuracy, while errors in the magnetic field, its linear gradient and the apparent velocity of the magnetic structure at the barycenter, are of second order in L/D , where L is the size of the S/C constellation and D is the characteristic scale of the magnetic structure.

To summarise this algorithm, we proceed as follows

(a) Estimate the magnetic field \mathbf{B}_c ; the first order magnetic gradient $(\nabla \mathbf{B})_c$, and the time variation rate $\left(\frac{\partial \mathbf{B}}{\partial t} \right)_c$ of the magnetic field, at the barycenter and under the linear approximation; as in Eqs. (7) and (8).

Estimate the gradient of the current density at the barycenter $\nabla \mathbf{j}(\mathbf{t}, \mathbf{r}_c)$, as in Eq. (10).

492 (b) Determine the apparent velocity \mathbf{V} using the time variation rate $\left(\frac{\partial \mathbf{B}}{\partial t}\right)_c$ of the
 493 magnetic field and the first order magnetic gradient $(\nabla \mathbf{B})_c$ and define the x_3
 494 coordinate with $\hat{\mathbf{x}}_3 = -\mathbf{V} / V$; determine the three characteristic directions
 495 $(\hat{\mathbf{x}}_1, \hat{\mathbf{x}}_2, \hat{\mathbf{x}}_3)$ using MRA, and define the coordinate base vector $\hat{\mathbf{x}}_1 = \frac{\hat{\mathbf{x}}_3 \times \hat{\mathbf{x}}_3}{|\hat{\mathbf{x}}_3 \times \hat{\mathbf{x}}_3|}$,
 496 such as to fix the Cartesian coordinates (x_1, x_2, x_3) in the spacecraft constellation
 497 reference frame.
 498 (c) Calculate the time variation rate $\frac{\partial}{\partial t}(\nabla \mathbf{B})_c$ of the linear magnetic gradient at the
 499 barycenter, so as to obtain the components of the quadratic magnetic gradient
 500 $(\nabla_3 \nabla \mathbf{B})_c$ and $(\nabla \nabla_3 \mathbf{B})_c$, as in Eqs. (22) and (23).
 501 (d) Combine Ampere's law and the first order gradient of the current density
 502 $\nabla \mathbf{j}(t, \mathbf{r}_c)$ to calculate the transverse quadratic magnetic gradient of B_3 , i.e.
 503 $\nabla_p \nabla_q B_3(p, q = 1, 2)$, as in Eq. (25).
 504 (e) Solve the equations $\frac{\partial}{\partial X_3} \frac{\partial}{\partial X_3} \hat{\mathbf{b}} = 0$, derived by MRA, so as to obtain the
 505 components: $\partial_2 \partial_2 B_p(p = 1, 2)$.
 506 (f) Determine the remaining four components of the quadratic magnetic gradient,
 507 $(\partial_1 \partial_2 B_p)_c = (\partial_2 \partial_1 B_p)_c$ and $(\partial_1 \partial_1 B_p)_c, (p = 1, 2)$, using the equation $\nabla(\nabla \cdot \mathbf{B}) = 0$
 508 derived from the divergence free condition of the magnetic field and the equation
 509 $\nabla(\nabla \times \mathbf{B}) = \nabla \mathbf{j}$ from Ampere's law, as in Eqs. (41) - (44).
 510 (g) Revise the magnetic field \mathbf{B}_c and the first order magnetic gradient $(\nabla \mathbf{B})_c$ with
 511 the quadratic magnetic gradient $G^{(2)} = (\nabla \nabla \mathbf{B})_c$ obtained initially, as in the formulas
 512 (46) and (47), and perform the above steps (b) - (f) once again, so as to get the

corrected quadratic magnetic gradient $(\nabla\nabla\mathbf{B})_c$, as well as the corrected apparent velocity \mathbf{V} of the magnetic structure.

It should be noted that, the magnetic field, the linear magnetic gradient and the quadratic magnetic gradient are all identical in different reference frames. We will test all these estimators in detail in Section 4.

Given the magnetic field \mathbf{B}_c , the first order magnetic gradient $(\nabla\mathbf{B})_c$ and the quadratic magnetic gradient $(\nabla\nabla\mathbf{B})_c$, the complete geometry of the magnetic field lines of the magnetic structure can be determined. We will find the estimators for the geometrical parameters of the MFLs in the next section.

3. Determining the complete geometry of magnetic field lines based on multiple S/C measurements

The geometry of the MFLs plays a critical role in the evolution of the space plasmas. In this section, we will extract the estimators for the complete geometry of the MFLs, from the linear and quadratic gradients of the magnetic field estimated in Section 2.

3.1 The natural coordinates and curvature of the MFLs

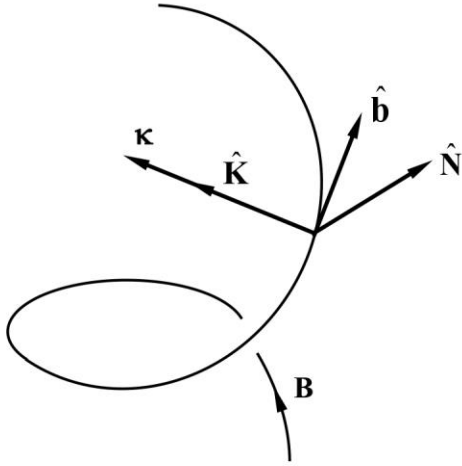


Figure 3. Demonstration on the geometry of the magnetic field lines. $\hat{\mathbf{b}} = \mathbf{B} / B$ is the magnetic unit vector; $\boldsymbol{\kappa}$ is the curvature vector of the magnetic field line, $\hat{\mathbf{K}}$ and $\hat{\mathbf{N}}$ are the principal normal and binormal, respectively. The magnetic field line is also twisting with torsion.

The directional magnetic unit vector is $\hat{\mathbf{b}} = \mathbf{B} / B$, which is also the tangential vector of the MFLs. The MFLs are usually turning, and the bending of MFLs is characterized by the curvature vector, i.e.,

$$\boldsymbol{\kappa} = \frac{d\hat{\mathbf{b}}}{ds} = (\hat{\mathbf{b}} \cdot \nabla) \hat{\mathbf{b}}, \quad (48)$$

where 's' is the arc length along the MFLs.

Shen et al., (2003, 2011) first presented the estimator of the curvature of MFLs, which has found many applications in multi-point data analysis. Here a brief description of it is given and we will then investigate further the complete geometry of the MFLs as well as the explicit estimators.

The gradient of the magnetic field $(\nabla \mathbf{B})_c$ at the barycenter from multi-spacecraft measurements has already been expressed in Section 2.

The gradient of the magnetic strength $B=|\mathbf{B}|$ is

$$\nabla_i B = \frac{1}{2B} \nabla_i B^2 = \frac{1}{B} B_j \nabla_i B_j, \quad (49)$$

while at the barycenter of the S/C constellation,

$$(\nabla_i B)_c = B_c^{-1} B_{cj} (\nabla_i B_j)_c. \quad (50)$$

Similarly, the gradient of the unit magnetic vector $\hat{\mathbf{b}}$ is

$$\nabla_i b_j = \nabla_i \frac{B_j}{B} = B^{-1} \nabla_i B_j - B^{-2} B_j \nabla_i B. \quad (51)$$

With Eq (49), the above formula (51) becomes

$$\nabla_i b_j = B^{-1} \nabla_i B_j - B^{-1} b_j b_m \nabla_i B_m. \quad (52)$$

Hence, the gradient of the unit magnetic vector $\hat{\mathbf{b}}$ at the barycenter is

$$(\nabla_i b_j)_c = B^{-1} (\nabla_i B_j)_c - B^{-1} b_j b_m (\nabla_i B_m)_c. \quad (53)$$

All the coefficients on the right hand side of the above formula involve values at the

barycenter (Shen, et al., 2003): $(B_i)_c = \frac{1}{N} \sum_{\alpha=1}^N B_{\alpha i}$, $(b_i)_c = B_{ci}/|\mathbf{B}_c|$. The formula (53)

obeys the condition that: $b_j (\nabla_i b_j)_c = 0$, which is required by the constraint

$$\hat{\mathbf{b}} \cdot \hat{\mathbf{b}} = 1.$$

The curvature of the MFLs at the barycenter is therefore

$$\kappa_{cj} = b_i (\nabla_i b_j)_c = B^{-1} b_i (\nabla_i B_j)_c - B^{-1} b_i b_j b_m (\nabla_i B_m)_c. \quad (54)$$

All the coefficients on the right hand side of the above formula involve values at the

barycenter. The formula (54) is the estimator of the curvature of the MFLs based on

the multi-S/C magnetic measurements. It is noted that there can be no field line

crossing through the point where $B=0$; thus, there is no need to calculate the curvature from formula (54). It is noted that formula (54) satisfies $\hat{\mathbf{b}}_c \cdot \boldsymbol{\kappa}_c = b_{cj} \kappa_{cj} = 0$, indicating that the obtained curvature vector is orthogonal to the magnetic field.

The radius of the curvature of the MFLs is

$$R_c = 1/\kappa_c. \quad (55)$$

The principal normal vector of the MFLs is

$$\hat{\mathbf{K}} = \boldsymbol{\kappa}_c / |\boldsymbol{\kappa}_c|. \quad (56)$$

The binormal vector of the MFLs is

$$\hat{\mathbf{N}} = \hat{\mathbf{b}} \times \hat{\mathbf{K}} = \frac{\hat{\mathbf{b}} \times \boldsymbol{\kappa}_c}{\kappa_c}, \quad (57)$$

The above expressions collectively describe the estimators of the magnetic curvature analysis approach [Shen et al., 2003; 2011], where $\{\hat{\mathbf{b}}, \hat{\mathbf{K}}, \hat{\mathbf{N}}\}$ constitute the natural coordinates, or the Frenet frame (trihedron). The unit magnetic vector $\hat{\mathbf{b}}$, principal normal $\hat{\mathbf{K}}$ and binormal $\hat{\mathbf{N}}$ are orthogonal to each other.

Usually, the MFLs not only bend, but also twist, such as the helical MFLs manifested in a flux rope. The twist of the MFLs can be described quantitatively by the torsion. In order to get the complete geometry of the MFLs, therefore, the torsion should be known. The torsion of the MFLs is defined as

$$\tau \equiv \frac{1}{\kappa} \frac{d^2 \hat{\mathbf{b}}}{ds^2} \cdot \hat{\mathbf{N}} = \frac{1}{\kappa} \frac{d\boldsymbol{\kappa}}{ds} \cdot \hat{\mathbf{N}} = -\frac{1}{\kappa} \boldsymbol{\kappa} \cdot \frac{d\hat{\mathbf{N}}}{ds}. \quad (58)$$

Therefore, the quadratic gradient of the magnetic field $\nabla \nabla \mathbf{B}$ is essential for the calculation of the torsion of the MFLs.

We now investigate the relationship between the torsion of the MFLs and the quadratic gradient of the unit magnetic vector $\nabla\nabla\hat{\mathbf{b}}$; as well as with the quadratic magnetic gradient $\nabla\nabla\mathbf{B}$.

To do this, we need to first deduce the expression of the quadratic gradient of the unit magnetic vector in terms of the linear and quadratic magnetic gradients.

The quadratic gradient of the unit magnetic vector $\hat{\mathbf{b}}$ is

$$\begin{aligned}\nabla_k \nabla_i b_j &= \nabla_k \left(B^{-1} \nabla_i B_j - B^{-1} b_j b_l \nabla_i B_l \right) \\ &= \nabla_k B^{-1} \cdot \nabla_i B_j + B^{-1} \nabla_k \nabla_i B_j - \nabla_k \left(B^{-1} b_j b_l \right) \cdot \nabla_i B_l - B^{-1} b_j b_l \nabla_k \nabla_i B_l \\ &= -B^{-2} \nabla_k B \cdot \nabla_i B_j + B^{-1} \nabla_k \nabla_i B_j + B^{-2} \nabla_k B \cdot b_j b_l \nabla_i B_l \\ &\quad - B^{-1} b_l \nabla_k b_j \cdot \nabla_i B_l - B^{-1} b_j \nabla_k b_l \cdot \nabla_i B_l - B^{-1} b_j b_l \nabla_k \nabla_i B_l \\ &= -B^{-2} \nabla_k B \cdot \nabla_i B_j + B^{-1} \nabla_k \nabla_i B_j + 3B^{-2} b_j b_l \nabla_k B \nabla_i B_l \\ &\quad - B^{-2} b_l \nabla_k B_j \nabla_i B_l - B^{-2} b_j \nabla_k B_l \cdot \nabla_i B_l - B^{-1} b_j b_l \nabla_k \nabla_i B_l.\end{aligned}\quad (59)$$

Thus the estimator of the quadratic gradient of $\hat{\mathbf{b}}$ at the barycenter is expressed as

$$\begin{aligned}\left(\nabla_k \nabla_i b_j \right)_c &= -B^{-2} \left(\nabla_k B \right)_c \left(\nabla_i B_j \right)_c + 3B^{-2} b_j b_m \left(\nabla_k B \right)_c \left(\nabla_i B_m \right)_c - B^{-2} b_m \left(\nabla_k B_j \right)_c \left(\nabla_i B_m \right)_c \\ &\quad - B^{-2} b_j \left(\nabla_k B_m \right)_c \cdot \left(\nabla_i B_m \right)_c + B^{-1} \left(\nabla_k \nabla_i B_j \right)_c - B^{-1} b_j b_m \left(\nabla_k \nabla_i B_m \right)_c.\end{aligned}\quad (60)$$

Based on this definition, the torsion of the MFLs is

$$\begin{aligned}\tau &= \frac{1}{\kappa} \frac{d\kappa}{ds} \cdot \hat{\mathbf{N}} = \frac{1}{\kappa} b_j \partial_j (b_k \partial_k b_i) N_i \\ &= \frac{1}{\kappa} \left(b_j \partial_j b_k \cdot \partial_k b_i + b_j b_k \partial_j \partial_k b_i \right) N_i.\end{aligned}\quad (61)$$

So that the torsion of the MFLs at the barycenter of the S/C constellation is

$$\tau_c = \kappa^{-1} N_i \cdot \left[b_j \left(\partial_j b_k \right)_c \cdot \left(\partial_k b_i \right)_c + b_j b_k \left(\partial_j \partial_k b_i \right)_c \right].\quad (62)$$

The above formula is one of the estimators of the torsion of the MFLs that is dependent on the linear and quadratic gradients of the unit magnetic vector $\hat{\mathbf{b}}$.

609

610 By substituting Eqs (52) and (59) into Eq (61), the torsion of the MFLs is obtained as

$$611 \quad \tau = \kappa^{-1} B^{-3} N_j B_i \partial_i B_k \partial_k B_j + \kappa^{-1} B^{-3} N_j B_k B_i \partial_k \partial_i B_j, \quad (63)$$

612 where the condition $b_j N_j = 0$ has been used. Appendix C presents another

613 verification of the expression (63) for clarity. It seems that the formula (63) is

614 invalid as $B=0$ or $\kappa = 0$. However, there is no field line as $B=0$, while for

615 $\kappa = 0$, the field line is a straight line and its torsion has no fixed value, and thus

616 is meaningless.

617 Therefore, the torsion of the MFLs at the barycenter can be written as

$$618 \quad \tau_c = \kappa^{-1} B^{-3} N_j B_i \left(\partial_i B_k \right)_c \left(\partial_k B_j \right)_c + \kappa^{-1} B^{-3} N_j B_k B_i \left(\partial_k \partial_i B_j \right)_c. \quad (64)$$

619 All the coefficients on the right hand side of the above formula involve values at

620 the barycenter. Formula (64) is another estimator of the torsion of the MFLs,

621 expressed in terms of the linear and quadratic gradients of the magnetic field.

622 The two different estimators of the torsion of the MFLs (62) and (64) are

623 obviously equivalent.

624

625 **4. Tests**

626

627 In this section, the estimators put forward in Sections 2 and 3 will be tested for

628 model current sheets and flux ropes, which can occur in the magnetosphere, in order

629 to verify the validity and accuracy of this approach. A one-dimensional Harris current

630 sheet model (Harris, 1962) and a Lundquist-Lepping cylindrical force-free flux rope

model (Lundquist, 1950) are used for these two typical structures, respectively. Appendices D and E present, analytically, the geometrical features of these two kinds of magnetic structures. The tests below have shown that the estimators of the quadratic magnetic gradients and the complete geometry of the MFLs are obtained with good accuracy compared to the models, so we expect they can find wide applications in investigating the magnetic structures and configurations in space plasmas with multi-S/C measurements.

4.1 The steps needed for this comparison

The operative calculating steps can be summarized as follows:

(a) Deriving the first-order gradients of \mathbf{B} and \mathbf{J} .

With four-point measurements, the temporal and spatial gradients of the magnetic field ($\nabla\mathbf{B}, \frac{\partial\mathbf{B}}{\partial t}$) and the current density ($\nabla\mathbf{J}, \frac{\partial\mathbf{J}}{\partial t}$) are readily deduced by the least-squares gradient calculation as outlined in Appendix A. The temporal variation $\frac{\partial\nabla\mathbf{B}}{\partial t}$ can also be inferred by differential calculations.

(b) Determining the velocity of the magnetic structures relative to the SCs.

Once the time series of $\nabla\mathbf{B}, \frac{\partial\mathbf{B}}{\partial t}$ are obtained, the velocity of the magnetic structures relative to the S/C constellation can be derived by Equation (15), $\frac{\partial\mathbf{B}}{\partial t} + \mathbf{V} \cdot \nabla\mathbf{B} = 0$. Therefore, the velocity of the spacecraft is $\mathbf{V}' = -\mathbf{V}$.

(c) Constructing the local coordinates $\{\hat{\mathbf{e}}_1, \hat{\mathbf{e}}_2, \hat{\mathbf{e}}_3\}$.

According to above statements, $\hat{\mathbf{e}}_3$ is defined as the direction of the relative velocity of the spacecraft to the magnetic structure, i.e., $\hat{\mathbf{e}}_3 = \frac{\mathbf{V}}{|\mathbf{V}|}$. We can then apply MRA

analysis to derive the minimum rotation direction of the magnetic field ($\hat{\mathbf{X}}_3$) and the $\hat{\mathbf{e}}_1$ can be set as $\hat{\mathbf{e}}_1 = \hat{\mathbf{X}}_3 \times \hat{\mathbf{e}}_3$. Finally, $\hat{\mathbf{e}}_2$ completes the right-handed system.

(d) Deriving $\nabla\nabla\mathbf{B}$ and $\nabla\nabla\hat{\mathbf{b}}$ and calculating the torsion of MFLs.

After expressing these parameters (\mathbf{B} , $\nabla\mathbf{B}$, $\nabla\mathbf{J}$, $\frac{\partial\nabla\mathbf{B}}{\partial t}$ and \mathbf{V}) in the local coordinates, we then can derive the quadratic gradient of magnetic field and the magnetic unit vector, $\nabla\nabla\mathbf{B}$ and $\nabla\nabla\hat{\mathbf{b}}$ by following the steps stated in Section 2. Furthermore, the torsion of magnetic field line can be obtained by Equation (62) or (64).

(e) Performing iterative operations to obtain more accurate results.

The estimates of the magnetic field and the first-order gradient of magnetic field at the barycenter of the four S/C can be modified by Equation (45) and (47), in order to repeat the same procedure as in steps (a)-(d) above.

4.2 One-dimensional Harris Current Sheet

For the one-dimensional Harris current sheet, the magnetic field can be formulated as Equation (D1) in Appendix D. In this test, the parameters of the current sheet are $B_0=50\text{nT}$, $B_y=10\text{nT}$, $B_z=20\text{nT}$, $h=R_E$. As shown in Figure 4a, we set an arbitrary S/C constellation trajectory from (2, 2, 2) R_E to (-2, -2, -2) R_E during 100 seconds. The S/C constellation is assumed to be a regular tetrahedron with a separation of $L=100$ km. The analytic values of the magnetic field and the current density at the barycenter of the four S/Cs are shown in panels (b) and (c) in Figure 4, respectively.

In this test, we have set $n=10$, and make $N=4n=40$ points to calculate the spatial and temporal gradient of the magnetic field at the barycenter of the S/C constellation with the method in Appendix A. Therefore, we can get the spatial gradient of the vector field within the interval 5-95s. Furthermore, the temporal and spatial scale corresponds to the time resolution of the field sampling (i.e. $T=1s$) and the characteristic size of tetrahedron ($L=100$ km). The magnetic field and the non-zero component $\frac{\partial B_x}{\partial z}$ of the linear magnetic gradient at the barycenter are derived with the formulas (5) and (6) and shown in Figure 4b and 4d, respectively, which are in good agreement with their analytic values as given by Appendix A (the circles represent the results derived by the method, while the black solid line denotes the analytic results derived by theoretical formula). The current density at the barycenter can also be derived with $\frac{\partial B_x}{\partial z}$ by Ampere's law ($\mathbf{j} = \nabla \times \mathbf{B}$) and is shown in Figure 4c. Those values are again consistent with the analytic values. The apparent velocity of the current sheet relative to the S/C constellation can be derived by formula (15). As shown in Figure 4e, the velocity V_z of S/C relative to the current sheet is within the range 252~260 km/s (0.0408~0.0398 Re/s), while the actual velocity is 257 km/s (0.0404 Re/s). Thus, the maximum relative error of the deduced velocity is $\frac{0.0006}{0.0404} \approx 1.5\%$, which is approximately the order of $L/h(\sim 0.016)$.

With the derived linear magnetic gradient and current density gradient, the quadratic magnetic gradient of this current sheet model can be readily obtained. It should be noted that, among the components of the quadratic magnetic gradient, only

$\frac{\partial^2 B_x}{\partial z^2}$ is non-zero, while $\frac{\partial^2 b_x}{\partial z^2}, \frac{\partial^2 b_y}{\partial z^2}, \frac{\partial^2 b_z}{\partial z^2}$ are non-zero among the components of

the quadratic gradient of magnetic unit vectors. The test is therefore focused on these components. Evidently, from Figure 4(g-j), there is extremely good agreement between the results obtained by the technique and the analytic values. As illustrated in Figure 4, $\frac{\partial^2 B_x}{\partial z^2}$ (Figure 4f) and $\frac{\partial^2 b_x}{\partial z^2}$ (Figure 4g) have bipolar signatures around the center of current sheet and are equal to zero at the center, while $\frac{\partial^2 b_y}{\partial z^2}$ (Figure 4h) and $\frac{\partial^2 b_z}{\partial z^2}$ (Figure 4i) show left-right symmetry around the current sheet center and reach a minimum at the center. These results are reasonable and in good agreement with the analytic results.

We have further obtained the geometry of the current sheet deduced by the method. The deduced curvature and torsion of the MFLs in the Harris current sheet are shown in Figure 4j and 4k. The magnetic curvature reaches a maximum at the center of current sheet, which indicates that the MFLs of the Harris current sheet bend most at the center. The torsion of the magnetic field line stays almost at zero, implying the MFLs in the Harris current sheet is planar (this agrees with the theoretical calculations in Appendix D). The order of the absolute error in the torsion is very small and less than $10^{-11} R_E^{-1}$. This check is a very good validation of the new method.

After completing the above steps, iterative operation and error analysis are necessary and we will discuss these later.

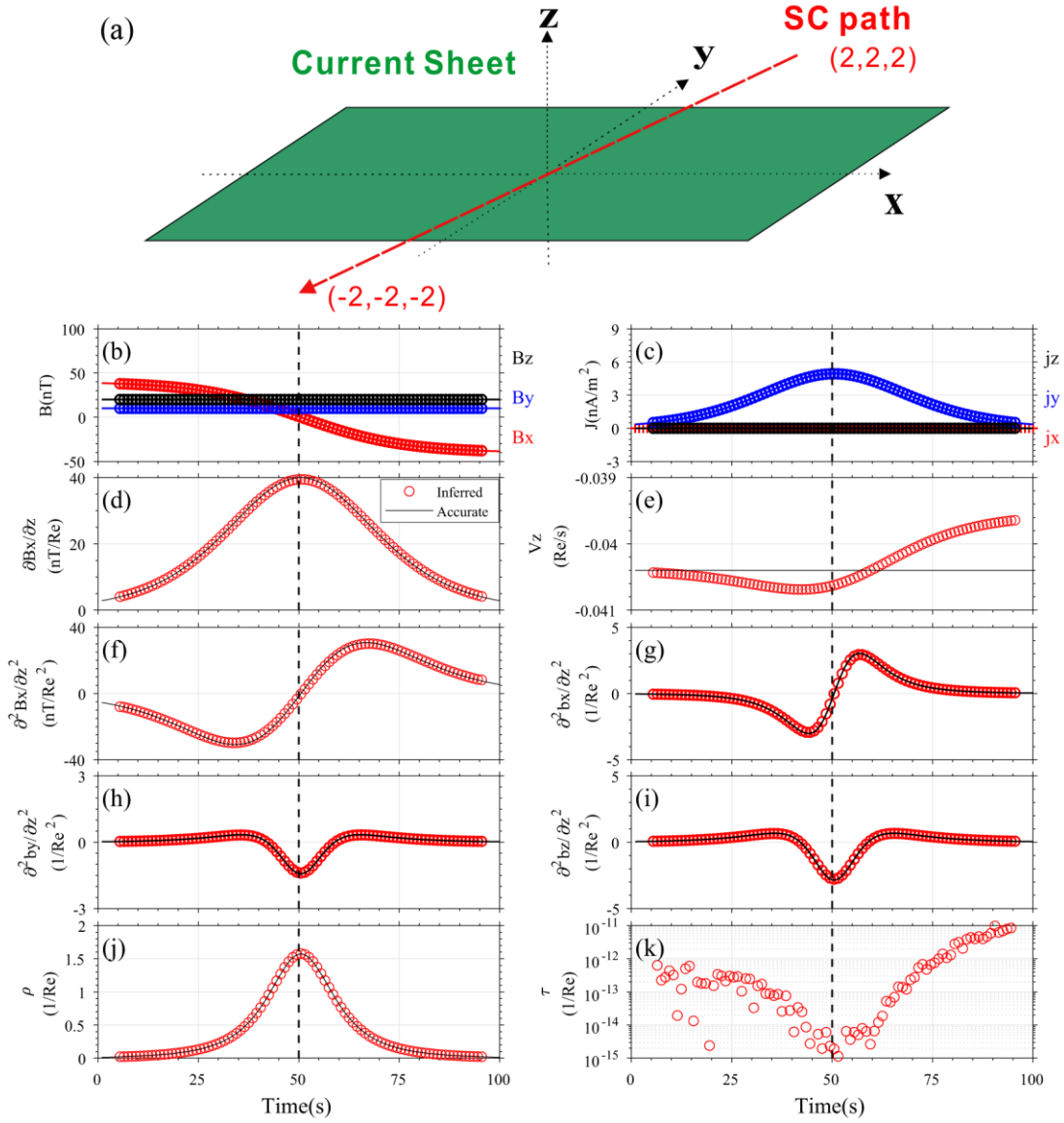


Figure 4: The comparison between the properties of 1-D Harris current sheet deduced from the estimators and those from the analytic calculations based on Appendix D. Panel (a) shows the current sheet configuration and the S/C trajectory in the current sheet reference frame; Panel (b), (c) show the variation of magnetic field and current density, respectively; Panel (d) is the time series of the gradient of magnetic field; Panel (e) denotes the relative velocity of S/Cs to the current sheet; Panel (f) represents the quadratic gradient of magnetic field; Panel (g), (h), (i) denote the time series of the quadratic gradient of unit magnetic vector b_x , b_y , b_z , respectively. The magnetic field

line curvature and torsion are displayed in Panel (j), (k), respectively. The vertical black dashed line in each panel represents the center of current sheet. The black solid lines in each panel are the accurate or theoretical results. The circles are the results obtained by the new method.

4.3 Two-dimensional Force-free Flux Ropes

In this section, we attempt to investigate the complete geometry of magnetic field lines for a classic force-free flux rope model. In this model, the three components of the magnetic vector in cylindrical coordinates can be expressed (Lundquist, 1950) as:

$$B_r = 0, B_\phi = B_0 J_1(\alpha r), B_z = B_0 J_0(\alpha r), \quad (65)$$

where r is the distance from the central axis, α is the characteristic scale of the flux rope, and J is the Bessel function. In this test, we adopt $B_0 = 60 \text{ nT}$, $\alpha = 1/R_E$, The trajectory of the SC is set to be from $(-2, 0, 0) R_E$ to $(2, 0, 0) R_E$ during 100 seconds and is shown in Figure 5a. The average magnetic field measured by four S/C is illustrated in Figure 5b, the bipolar signature of B_y and the enhancement of B_z around the flux rope's center is apparent.

By repeating the same procedures as in Section 4.2, the quadratic magnetic gradient can be readily acquired (Figure 5c, 5d, 5e, 5f, 5g). One can find that the results derived by the method are in good agreement with the analytic results obtained in Appendix E. The variations of curvature and torsion of the MFLs confirm that the magnetic topological structure is different from those of the current sheet (Figure 5h,

5i). It can also be seen from Figure 5h and 5i that the curvature of the MFLs contains a minimum, and the torsion of the MFLs contains a maximum, at the center. This indicates that the straighter and more twisted the MFLs, the nearer to the center of flux rope, implying the non-planar and helical structure of the flux rope. This test shows that the results obtained by the approach are in good agreement with the analytical results, indicating that the estimators obtained in Sections 2 and 3 are reliable and applicable.

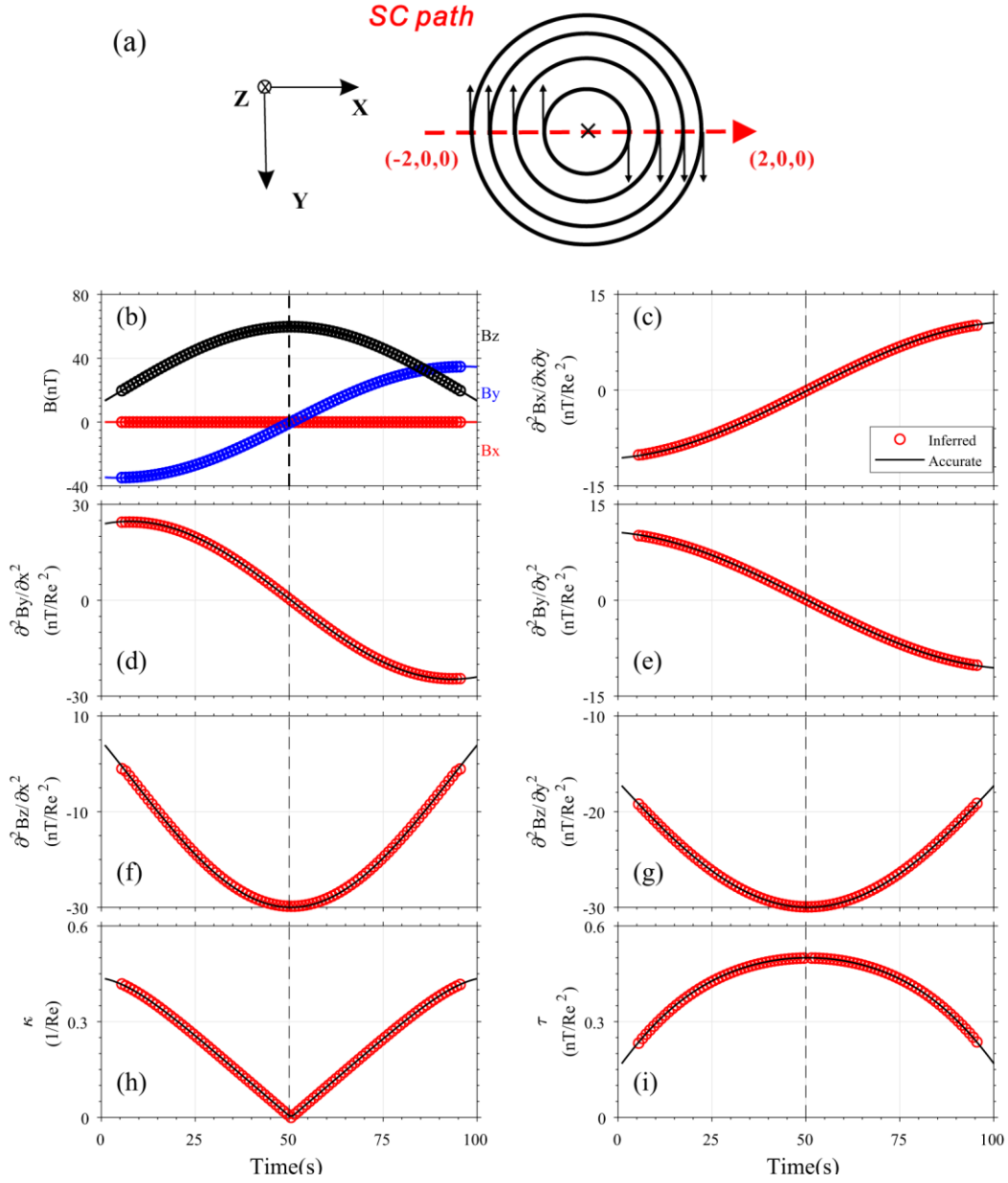


Figure 5: The properties of MFLs of 2-D flux rope. The relative path of S/Cs to the magnetic structure is sketched in Panel (a). Panel (b) shows the variation of the magnetic field; Panel (c), (d), (e), (f), (g) denote the time series of the quadratic gradient of magnetic field. The magnetic field line curvature and torsion are displayed in Panel (h) and (i). The vertical black dashed line in each panel represents the center

of flux rope. The circles and black solid lines represent the results inferred by our method and the accurate results, respectively.

4.4 Error Analysis

The errors of the estimators put forward in this study may arise from two types of sources: the underlying measurement errors and the truncation errors. The key measurement errors include the error in the measured magnetic field \mathbf{B} and that of the current density \mathbf{j} derived from the plasma moment data (which will be seen in the application in Section 5). The truncation errors arise from terms beyond the differential order considered here and represent neglected behaviour of the magnetic structure and plasmas.

The spatial truncation errors can be approximately measured by L/D , where D is the typical spatial size of magnetic structure and L is the size of tetrahedron of four SC. When L/D is very small, the truncation errors are generally small. However, as L/D grows large, the truncation errors may become significant. The iterative operation allows us to attempt to get more accurate and reliable results.

Figure 6 compares the results of the calculations made with no iteration; with the first and second iterations, and theoretical calculation with $L/D=0.3$. It can be seen that the iterations yield more accurate results. However, the second iteration in these examples did not produce better results than the first iteration.

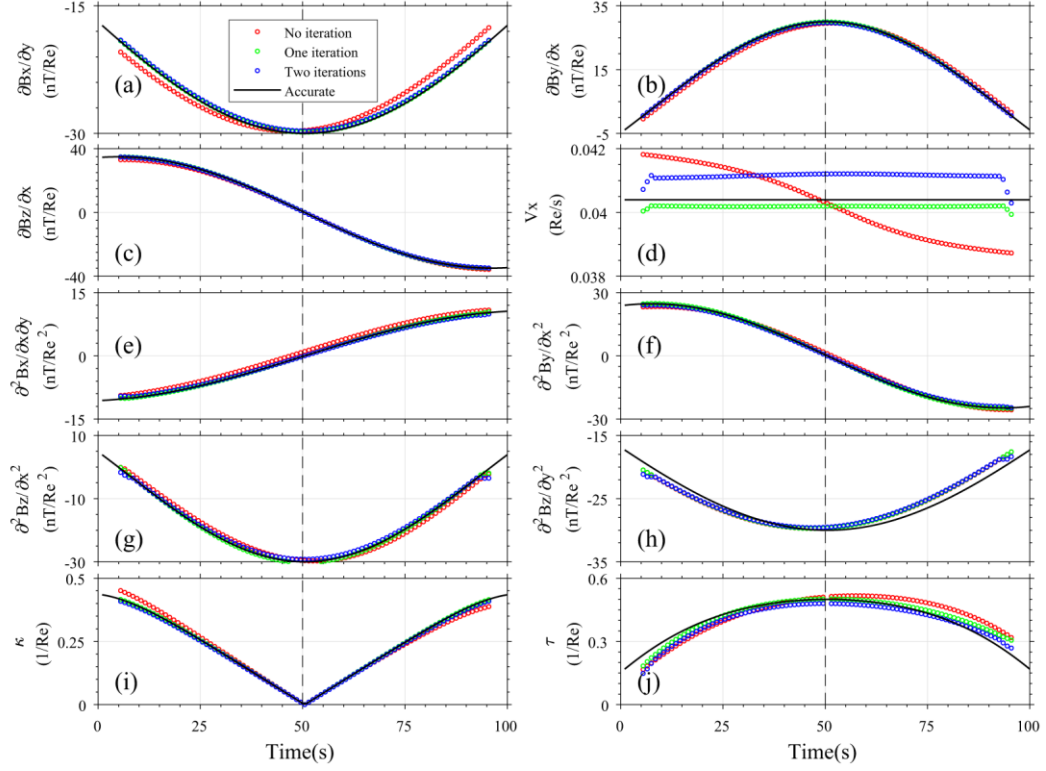


Figure 6: The comparison of those results with no iteration, first iteration and second iteration. The format of this figure is just the same as that of Figure 5. The red circles in each panel denote the result of no iteration, while the green and blue circles mark the result from the first iteration and second iteration, respectively. The black solid lines represent analytic results.

Figure 7 displays the variations of the relative errors of the results with L/D . The relative error is defined as $\langle |\frac{X_{\text{method}} - X_{\text{real}}}{X_{\text{real}}} | \rangle$, where X_{method} represents the results obtained with our method and X_{real} denotes the analytical results from the model. It is seen from Figure 7(a), (b), (c), (d), (e) that the relative errors of the linear magnetic gradient, apparent velocity and curvature of the MFLs are of first order in L/D for no

iteration calculations, but they are of second order in L/D after the first and second iterations. Nevertheless, the relative errors of the components of the quadratic magnetic gradient and the torsion of MFLs are all of first order in L/D (Figure 7f, g, h, I, j), although after the first or second iterations they are improved.

Through the above analysis, one can conclude that the most accurate results are those derived by at least one iteration, especially when L/D is larger than 0.5. Thus, it is necessary to perform the first iteration when L/D is larger than 0.5.

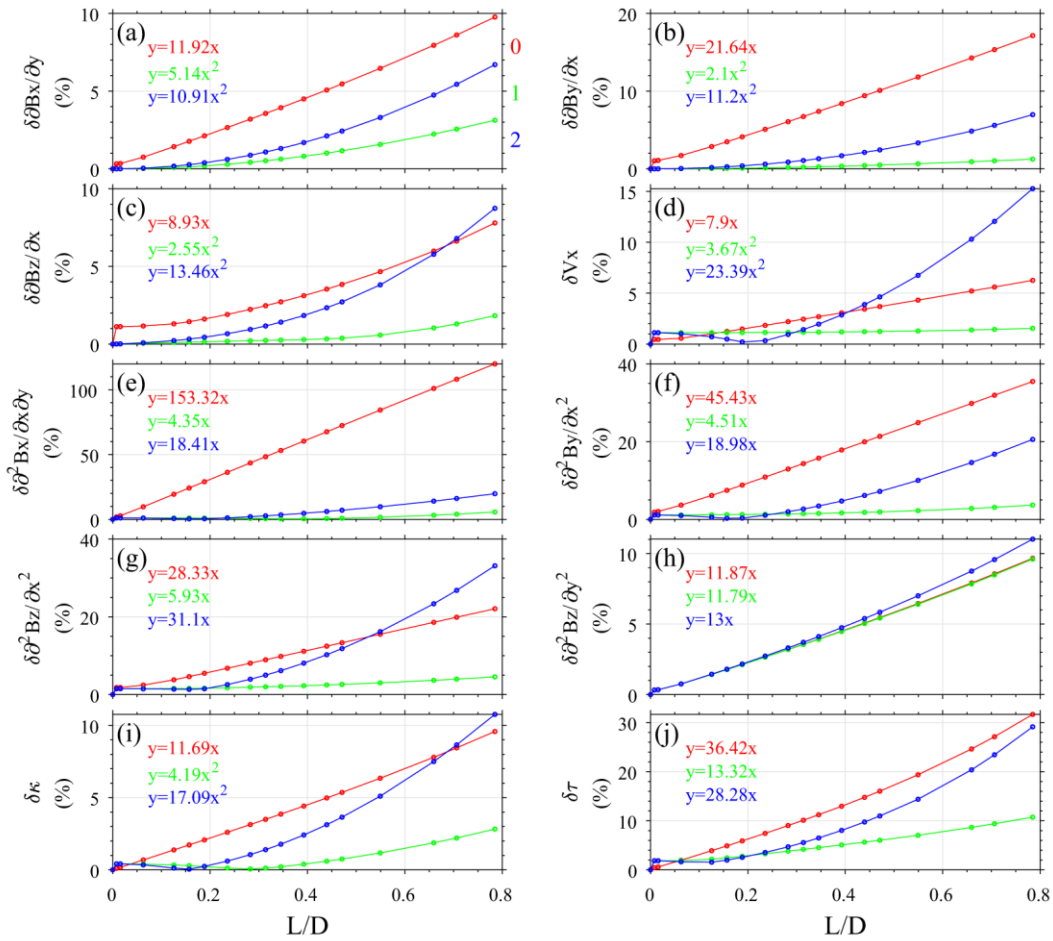


Figure 7: The relative errors (y) of the various calculated parameters of the flux rope for different L/D (x). The red solid lines in each panel are the calculation results with no iteration, while the green, blue lines represent the calculation results with the first

and second iterations, respectively. The format of this figure is the same as that of Figure 5.

5. Application: Magnetic Flux Rope

In this section, we have applied the approach developed in Sections 2 and 3 to investigate the magnetic structure and geometry of a magnetic flux rope at magnetopause, observed by MMS during 2015-10-16 13:04:33-13:04:35, which is the second of two sequential flux ropes reported by Eastwood et al., (2016), and has been analyzed by many researchers (e.g., Zhang et al., 2020). Here, we have used the high-resolution magnetic field data measured by the fluxgate magnetometer, operating at 128 vectors per second in burst-mode (Russell et al. 2014; Burch et al. 2015), and the plasma data provided by FPI (Fast Plasma Investigation, measuring electrons at cadence of 30ms and ions at cadence of 150 ms) (Torbert, et al. 2015; Pollock et al. 2016). To calculate the quadratic magnetic gradient, the plasma moments are interpolated to obtain a 1/128 s time resolution to match that of the magnetic field data and to derive the current density. Note that the MMS constellation is often nearly a regular tetrahedron with its separation scale of $L \approx 20$ km during this time interval.

Typically, there are many waves affecting the magnetic field at various frequencies in space plasmas. If we calculated the time variation rates of the magnetic field and the linear and quadratic magnetic gradients directly, the errors caused by these waves would be so large that we would miss the underlying global features of

the magnetic structure. To get rid of the influence of the waves, the magnetic field (Figure 8a) and current density (Figure 8b-8d) data have been filtered by a low-pass filter to eliminate disturbances with frequencies higher than 1Hz from the data. In order to apply the method in Appendix A to calculate the temporal and spatial gradients of the magnetic field and current density, we have adopted $n=10$ time points on each spacecraft to form a set of data. Thus, there are in total $N=4n=40$ points in a group of data. With this approach, the calculated temporal and spatial gradients of the magnetic field and current density have rather high accuracy.

We have derived the magnetic rotation features of the flux rope by using the MRA method illustrated in Appendix B (Shen et al., 2007). Figure 8e shows the time series of the magnetic minimum rotation direction $\hat{\mathbf{X}}_3$, which is approximately stable and nearly parallel to GSE +Y direction. Assuming the flux rope is cylindrically symmetric, $\hat{\mathbf{X}}_3$ could be approximately regarded as the orientation $\hat{\mathbf{n}}$ of the flux rope axis, i.e., $\hat{\mathbf{n}} = \hat{\mathbf{X}}_3$. The helical angle of the MFLs can be defined as $\beta = \text{asin}(\hat{\mathbf{b}} \cdot \hat{\mathbf{n}})$. As shown in Figure 8f, the helical angle β reaches its maximum value ($\sim 89^\circ$) at the time $\sim 34.1\text{s}$, implying that the MFLs lie basically along the axis orientation in the central part of the flux rope. The apparent velocity of the flux rope can be calculated by formula (17), and is illustrated in Figure 8g. One can find that, the apparent velocity at the leading edge of flux rope is larger than that at the trailing edge, suggesting that the flux rope is decelerating and not stable during this interval. Assuming that the flux rope is steady and has a force-free magnetic field, Eastwood et al., (2016) have derived the parameters of this flux rope, and estimate that the velocity

is $[-206.976, -19.8, -162.88]$ km/s in GSE, as derived by timing analysis, the axis orientation is $[-0.012, 0.989, -0.149]$ in GSE and the radius is ~ 550 km. From our analysis, it is shown that the mean velocity is $\sim [-141.408, -47.58, -96]$ km/s and the axis orientation is $[-0.0889, 0.9367, -0.3386]$ in GSE during the interval (13:04:33.5-13:04:35), when the flux rope is nearly steady. Considering the complicated motion and structure of flux rope and the different data processing approaches applied, the small discrepancy among the results is not surprising.

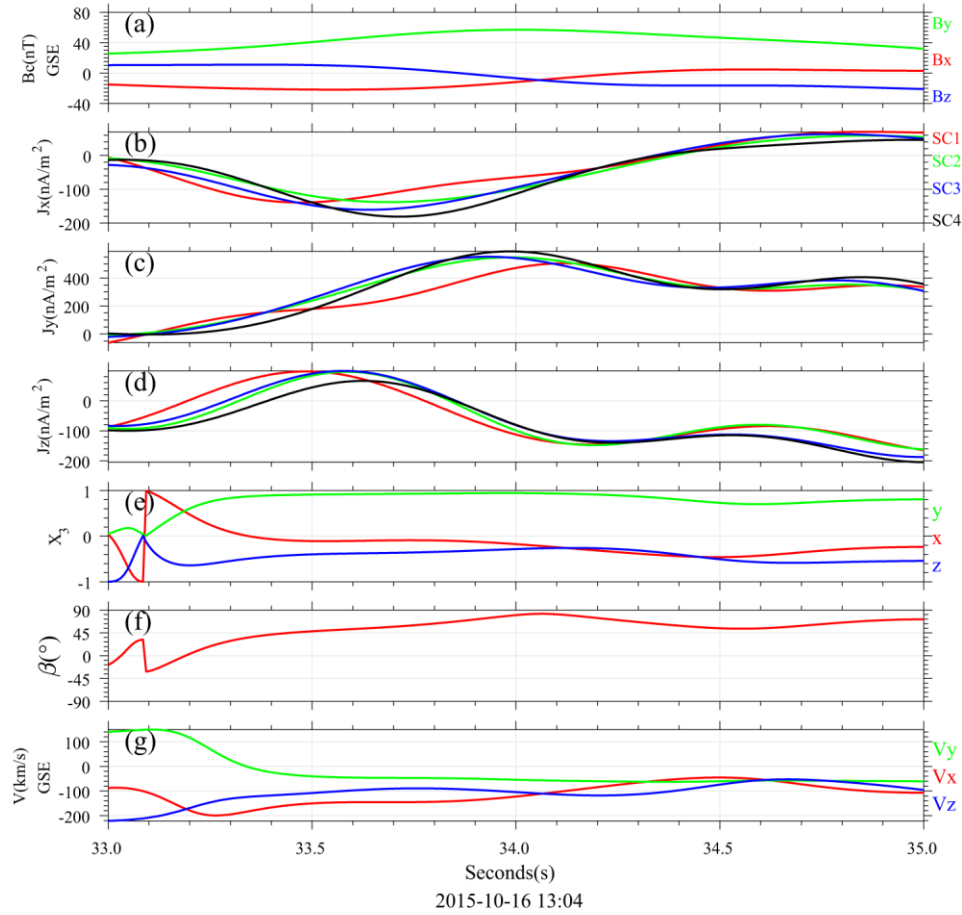


Figure 8: The parameters of the flux rope observed by MMS3 on 16 Oct. 2015. Panel (a) shows the magnetic field at the barycenter of tetrahedron; Panel (b), (c) and (d) display the components of the current density at the four S/C derived by plasma data;

Panel (e) denotes the minimum rotation direction of the MFLs, which is approximately the axis direction of the flux rope; Panel (f) represents the variation of the helical angle; Panel (g) shows the apparent velocity of the flux rope relative to the MMS constellation.

By using the estimators in Sections 2 and 3, the magnetic gradients and geometry of the flux rope can be obtained and these are demonstrated in Figure 9. The total 27 components of the quadratic gradient of magnetic field have been obtained with the estimators in Section 2, which are illustrated in panels (a)-(i) of Figure 9. It can be found that the order of the quadratic gradient of the magnetic field is generally less than 10^{-2} nT/km², while that of the first-order magnetic gradient is $\sim 10^{-1}$ nT/km. The complete geometry of the MFLs in the flux rope can be derived by the estimators in Section 3, which is illustrated in Figure 9j-l. It can be seen that the curvature of MFLs reaches its minimum value of $\sim 0.80 \times 10^{-3}$ /km (Figure 9j) and the torsion reaches its maximum value of ~ 0.012 /km² (Figure 9l) at ~ 34.1 sec, when the helical angle is the largest (Figure 8f). These features indicate that this flux rope is a typical one and is consistent with the 2-D flux rope model in Appendix E. The maximum curvature of the MFLs is about $\sim 3.0 \times 10^{-3}$ /km, while accordingly the minimum radius of the curvature of the MFLs is ~ 330 km. We can choose this as the characteristic scale of the flux rope, i.e., $D=330$ km. Furthermore, assuming the flux rope has a cylindrical helical structure, the torsion of MFLs can also be obtained directly from the curvature and helical angle from formula E9 in Appendix E. From Figure 9l, it can be seen that

the results obtained by both techniques show good agreement with each other.

Obviously, the magnetic field lines in this flux rope are right-hand spirals generally.

These results verify the effectiveness and applicability of the estimators given in

Sections 2 and 3. Since $L/D \approx 20/330 \approx 0.06$, we do not need to perform the iteration in

this case because the accuracy of the linear results with no iteration is already very

high.

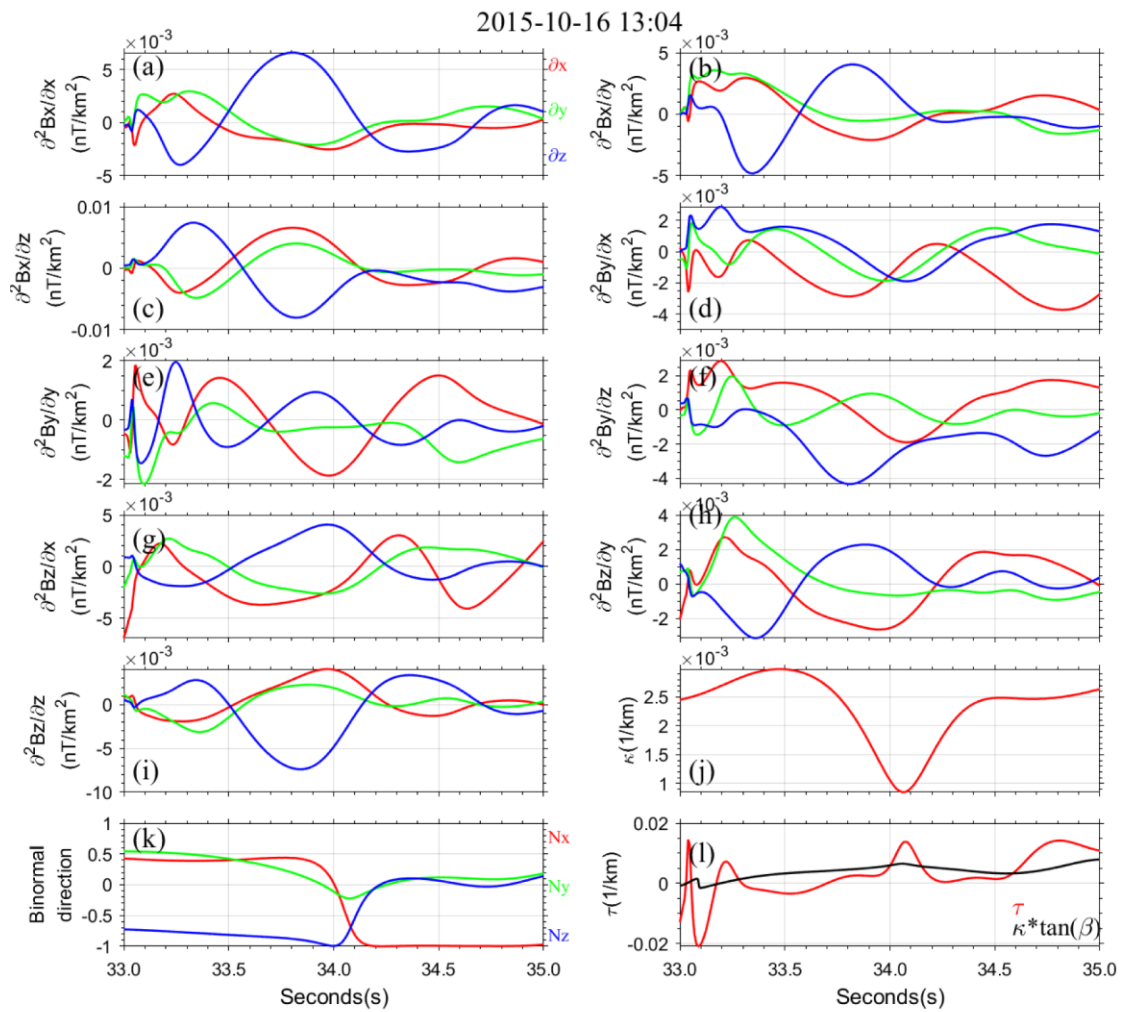


Figure 9: The magnetic structure of the flux rope on 16 Oct. 2015. Panel (a)-(i) show

all the 27 components of the quadratic gradient of magnetic field, where the red, green

and blue lines represent the partial derivative $\partial x, \partial y, \partial z$, respectively; Panel (j) gives

the time series of the curvature of the MFLs; Panel (k) represents the binormal direction of the MFLs; Panel (l) shows the torsion of the MFLs, with its value calculated by the magnetic gradients represented by the red line, and that drawn from the cylindrical symmetry approximation denoted by the black line.

6. Summary and Discussions

The quadratic magnetic gradient is a key parameter of the magnetic field, with which the fine structure of a magnetic structure can be revealed; as well as the twisting property of the magnetic field. However, up to now, the quadratic magnetic gradient from multi-S/C constellation measurements has not been explicitly calculated. Chanteur (1998) showed that in order to get the quadratic magnetic gradient from multi-point magnetic observations, in general, the number of S/C in the constellation has to be equal to or larger than 10, which is difficult to realize in present space exploration. Fortunately, the MMS constellation can not only provide rather accurate 4-point magnetic field, but can also produce very good 4-point current density estimates from particle measurements, such as to allow the quadratic magnetic gradient problem to be solved in the manner discussed here.

This paper provides a method to obtain the linear and quadratic magnetic gradients as well as the apparent velocity of the magnetic structure based on the 4 point magnetic field and current density observations and give their explicit estimators. Furthermore, the complete geometry of the magnetic field lines is

revealed on the bases of these linear and quadratic magnetic gradients, and the estimator for the torsion of the MFLs is given. Simple, but relevant, tests on this novel algorithm have been made for a Harris current sheet and a force-free flux rope model, and the effectiveness and accuracy of these estimators have been verified.

In this approach, the physical quantities to be determined are as follows: the magnetic field \mathbf{B}_c (3 parameters); the linear magnetic gradient $(\nabla\mathbf{B})_c$ (9 parameters); quadratic magnetic gradient $(\nabla\nabla\mathbf{B})_c$ ($6 \times 3 = 18$ parameters), and the apparent velocity of the magnetic structure \mathbf{V} (3 parameters); resulting in a total of $3+9+18+3=33$ undetermined parameters.

On the other hand, the input conditions for this algorithm are: the time series of magnetic field $\mathbf{B}_\alpha(t)$ at 4 points ($3 \times 4 = 12$ parameters); the transformation relationships $\frac{\partial\mathbf{B}}{\partial t} = -\mathbf{V} \cdot \nabla\mathbf{B}$ (3 independent constraint equations) and $\frac{\partial}{\partial t}\nabla\mathbf{B} = -\mathbf{V} \cdot \nabla\nabla\mathbf{B}$ ($3 \times 3 = 9$ independent constraint equations); the formula $\nabla(\nabla \times \mathbf{B}) = \nabla\mathbf{j}$, derived from Ampere's law ($2 \times 3 - 1 = 5$ independent constraints); the equation $\nabla(\nabla \cdot \mathbf{B}) = 0$, from the solenoidal condition of the magnetic field ($3 - 1 = 2$ independent constraints), and finally the constraint equations $\frac{\partial}{\partial X_3} \frac{\partial}{\partial X_3} b_p = 0$, as deduced from MRA (2 independent constraints); resulting in a total of $12+3+9+5+2+2=33$ independent parameters or constraints.

We note that the contribution of the current density measurements in this approach is the first order gradient of the current density, which is related to the quadratic magnetic gradient by Ampere's law. Considering the conservation of the

current density $\nabla \cdot \mathbf{j} = 0$ and $\partial_3 \nabla \mathbf{B}$ already obtained from the constraint equation $\frac{\partial}{\partial t} \nabla \mathbf{B} = -\mathbf{V} \cdot \nabla \nabla \mathbf{B}$, the constraint equation $\nabla(\nabla \times \mathbf{B}) = \nabla \mathbf{j}$ yields only $2 \times 3 - 1 = 5$ independent constraints ($\partial_3(\nabla \times \mathbf{B}) = \partial_3 \mathbf{j}$ is not independent). Similarly, $\nabla(\nabla \cdot \mathbf{B}) = 0$ provides only $3 - 1 = 2$ independent constraints.

Therefore, the linear and quadratic magnetic gradients, and the apparent velocity of the magnetic structure, can be completely determined based on the 4-point magnetic field and current density measured by the MMS constellation.

The calculations have been expressed as being carried out in the S/C constellation frame. The algorithm proceeds as follows. Firstly, under the linear approximation, the temporal and spatial gradients of the magnetic field ($\nabla \mathbf{B}, \frac{\partial \mathbf{B}}{\partial t}$) and of the current density ($\nabla \mathbf{j}, \frac{\partial \mathbf{j}}{\partial t}$) at the barycenter of the S/C constellation can be obtained by the least-squares gradient calculations as demonstrated in Appendix A.

The time rate of change of the linear magnetic gradient, $\frac{\partial}{\partial t}(\nabla \mathbf{B})_c$, and the second order time derivative of the magnetic field can also be obtained. The apparent velocity of the magnetic structure relative to the S/C frame system can then be readily obtained with the formula $\frac{\partial \mathbf{B}}{\partial t} = -\mathbf{V} \cdot \nabla \mathbf{B}$, and also the gradient of the linear magnetic gradient along the direction of motion, $(\nabla_3 \nabla \mathbf{B})_c$. With the constraint equation $\nabla(\nabla \times \mathbf{B}) = \nabla \mathbf{j}$, the transverse quadratic magnetic gradient of the longitudinal magnetic field B_3 , $\nabla_p \nabla_q B_3$ ($p, q = 1, 2$), can be found. Finally, the transverse quadratic magnetic gradients of the transverse magnetic field, $\partial_p \partial_q B_s(t, \mathbf{r}_c)$, can be obtained by using the constraint equations $\nabla(\nabla \cdot \mathbf{B}) = 0$, $\nabla(\nabla \times \mathbf{B}) = \nabla \mathbf{j}$, and magnetic rotation feature

962 $\frac{\partial}{\partial \mathbf{X}_3} \frac{\partial}{\partial \mathbf{X}_3} \mathbf{b}_p = 0$. Therefore, all the 18 independent components of the quadratic

963 magnetic gradient can be calculated.

964 The quadratic magnetic gradient, obtained with no iteration, has a truncation
965 error of the first order in L/D because the linear approximation has been made. To
966 find a more accurate quadratic magnetic gradient, an iterative procedure can be
967 performed. In this procedure, the magnetic field, the linear magnetic gradient, and the
968 time derivative of the linear magnetic gradient are corrected by using the quadratic
969 magnetic gradient calculated initially and the above steps are then repeated so as to
970 achieve the components of the corrected quadratic magnetic gradient. After this first
971 iteration, the magnetic field, linear magnetic gradient, the apparent velocity of the
972 magnetic structure at the barycenter of the S/C tetrahedron all have their accuracies
973 improved significantly and have truncation errors in the second order of L/D , while
974 the accuracy of the quadratic magnetic gradient obtained is also enhanced.

975 This algorithm is valid for both steady and unsteady structures, whether the
976 magnetic structures are moving at a constant velocities or accelerating /decelerating. It
977 is noted that the magnetic field, linear and quadratic magnetic gradients are identical
978 for different inertial frames of reference.

979 With the magnetic field, linear and quadratic magnetic gradients found, the
980 complete geometry of the MFLs can be determined, including the natural coordinates
981 or Frenet coordinates (tangential unit vector, principal normal and binormal),
982 curvature and torsion. The corresponding estimators for the geometrical features have
983 been given.

The algorithm for estimating the quadratic magnetic gradient and the geometry of the MFLs have been tested with the Harris current sheet and cylindrical flux rope, and its correctness has been verified. It is found that, the errors of the linear quadratic magnetic gradients, apparent velocity of the magnetic structure, and the geometrical parameters are of first order in L/D when no iteration is made. If one iteration is performed, the accuracies of the linear magnetic gradient, apparent velocity of the magnetic structure, curvature of the MFLs are improved significantly and their errors appear at the second order in L/D , while the accuracies of the quadratic magnetic gradient and the torsion of the MFLs are also enhanced. To determine the first order magnetic gradient and apparent relative velocity of the magnetic structure, this algorithm is more accurate than the previous approaches based on the linearity approximation (Harvey, 1998; Chanteur, 1998; Shi et al., 2006).

We have also applied the algorithm developed in this research to investigate the magnetic structure of one flux rope measured by MMS (Eastwood et al., 2016), showing good results. The applicability of this approach is therefore verified.

If the magnetic gradients with orders higher than two are neglected the magnetic field can be expressed as

$$\mathbf{B}(\mathbf{t}, \mathbf{r}) = \mathbf{B}(\mathbf{t}, \mathbf{r}_c) + (\mathbf{r} - \mathbf{r}_c) \cdot \nabla \mathbf{B}(\mathbf{t}, \mathbf{r}_c) + \frac{1}{2} (\mathbf{r} - \mathbf{r}_c) (\mathbf{r} - \mathbf{r}_c) \cdot \nabla \nabla \mathbf{B}(\mathbf{t}, \mathbf{r}_c). \quad (65)$$

With the MMS magnetic field and current density measurements, the linear and quadratic magnetic gradients at the barycenter are obtained, such that the local spatial distribution of the magnetic field, as well as the MFLs, can be obtained.

1006

1007

1008 **Acknowledgments.** This work was supported by National Natural Science

1009 Foundation (NSFC) of China Grant (No. 41874190, 41922031 and 41774188). M. W.

1010 Dunlop is partly supported by Science & Technology Facilities Council (STFC)

1011 research grant ST/M001083/1, the NSFC grants 41574155 and 41431071, and the

1012 Natural Environment Research Council (NERC) grant NE/P016863/1. The authors are

1013 also thankful to the entire MMS team for providing the MMS data

1014 (<https://cdaweb.gsfc.nasa.gov>).

1015

1016

1017

1018

1019

1020

1021

1022

1023

1024

1025

1026

1027

Appendix A: The explicit estimators for the linear gradients of field in space and time

De Keyser, et al. (2007) has put forward an algorithm for calculating the gradients in space and time of a field, which they called Least-Squares Gradient Calculation (LSGC). Here we will find the explicit estimator of the 4 dimensional linear gradients of a scalar field or one component of the vector field.

Considering the 4 S/C of the constellation obtained time series of measurements on a certain physical quantity investigated, as illustrated in Figure 1 in Section 2. Here the S/C constellation reference frame is used. Assuming each S/C makes observations at n times, in total $N=4n$ measurements are made by the constellation, which form a set of data. (It is supposed that, in this area of space time, the physical quantity concerned is approximately varying linearly, and the linear gradients of field in space and time are about homogeneous [De Keyser, et al., 2007].) In the S/C constellation coordinate system, the position of the observation point is

$x_{(a)}^\mu = (x_a, y_a, z_a; t_a) (\mu = 1, 2, 3, 4)$. It is convenient to use the dimensionless length and time in the investigation. If the characteristic size of the S/C constellation is L and the time resolution of the observations is T , we can make the transformation:

$x_a / L \rightarrow x_a, t_a / T \rightarrow t_a$. Obviously, in the S/C constellation reference frame, the four

1049 S/C are nearly motionless and their space coordinates $x_{(a)}^i = (x_a, y_a, z_a)$ do not
 1050 change with time during typical structure crossing events.

1051

1052 In the S/C constellation reference frame, at the space time

1053 $x_{(a)}^\mu = (x_a, y_a, z_a; t_a) (\mu = 1, 2, 3, 4)$, the physical quantity measured is $f(x_a^\mu) = f_{(a)}$, its

1054 gradients are $\frac{\partial f}{\partial x^\mu} = \nabla_\mu f \equiv \left(\frac{\partial f}{\partial x}, \frac{\partial f}{\partial y}, \frac{\partial f}{\partial z}, \frac{\partial f}{\partial t} \right)$. The spacetime coordinates at the

1055 central point satisfy

$$1056 \quad \sum_{a=1}^N \Delta x_{(a)}^\mu = \sum_{a=1}^N (x_{(a)}^\mu - x_c^\mu) = 0. \quad (\text{A1})$$

1057 Thus the spacetime coordinates at the central point are

$$1058 \quad x_c^\mu = \frac{1}{N} \sum_{a=1}^N x_{(a)}^\mu. \quad (\text{A2})$$

1059 Here x_c^i are the space coordinates of the barycenter of the S/C constellation, which

1060 have fixed values and can be chosen as $x_c^i = 0$. $x_c^4 = t_c$ is the average time of the 4n

1061 observations.

1062

1063 The physical quantity $f_{(a)}$ measured at the point $x_{(a)}^\mu$ can be expanded around

1064 the central point x_c^μ as (Taylor expansion)

$$1065 \quad f_{(a)} = f_c + \Delta x_a^\nu \nabla_\nu f_c + \frac{1}{2} \Delta x_a^\nu \Delta x_a^\lambda \nabla_\nu \nabla_\lambda f_c \quad (\text{A3})$$

1066 Or

$$1067 \quad f_{(a)} = f_c + \Delta x_a^\nu G_\nu + \frac{1}{2} \Delta x_a^\nu \Delta x_a^\lambda G_{\nu\lambda} \quad (\text{A3}')$$

1068 Here, the first order gradient $G_\nu = (\nabla_\nu f)_c$, and the quadratic gradient

1069 $G_{\nu\lambda} = (\nabla_\nu \nabla_\lambda f)_c$. there are 5 parameters $(f_c, G_\nu = (\nabla_\nu f)_c)$ to be determined.

1070 Construct the action

$$1071 \quad S = \frac{1}{N} \sum_a \left[f_c + \Delta x_{(a)}^\nu G_\nu + \frac{1}{2} \Delta x_{(a)}^\nu \Delta x_{(a)}^\lambda G_{\nu\lambda} - f_{(a)} \right]^2 \quad (A4)$$

1072 To minimize it, let

$$1073 \quad \delta S = 0 \quad (A5)$$

1074 Such as to obtain f_c and $G_\nu = \nabla_\nu f_c$ at the central point. The above equation leads to

$$1075 \quad \frac{\partial S}{\partial f_c} = 0, \frac{\partial S}{\partial G_\nu} = 0, \frac{\partial S}{\partial G_{\nu\lambda}} = 0. \quad (A6)$$

1076 Since

$$1077 \quad \begin{aligned} \frac{\partial S}{\partial f_c} &= \frac{1}{N} \sum_{a=1}^N 2 \left[f_c + \Delta x_{(a)}^\nu G_\nu + \frac{1}{2} \Delta x_{(a)}^\nu \Delta x_{(a)}^\lambda G_{\nu\lambda} - f_{(a)} \right] \\ &= 2 \cdot \frac{1}{N} \sum_{a=1}^N [f_c - f_{(a)}] + 2 \cdot \frac{1}{N} \sum_{a=1}^N \Delta x_{(a)}^\nu G_\nu + \frac{1}{N} \sum_{a=1}^N \Delta x_{(a)}^\nu \Delta x_{(a)}^\lambda G_{\nu\lambda} = 0 \end{aligned} \quad (A7)$$

1078 Considering Equation (A1), it reduces to

$$1079 \quad f_c = \frac{1}{N} \sum_a f_{(a)} - \frac{1}{2N} \sum_a \Delta x_{(a)}^\nu \Delta x_{(a)}^\lambda G_{\nu\lambda}. \quad (A8)$$

1080 or

$$1081 \quad f_c = \frac{1}{N} \sum_a f_{(a)} - \frac{1}{2} R^{\nu\lambda} G_{\nu\lambda}. \quad (A8')$$

1082 Where the general volume tensor $R^{\mu\nu}$ is defined as

$$1083 \quad R^{\mu\nu} \equiv \frac{1}{N} \sum_{a=1}^N \Delta x_{(a)}^\mu \Delta x_{(a)}^\nu = \frac{1}{N} \sum_{a=1}^N (x_{(a)}^\mu - x_c^\mu) (x_{(a)}^\nu - x_c^\nu). \quad (A9)$$

1084 Furthermore,

$$1085 \quad \begin{aligned} 0 = \frac{\delta S}{\delta G_\mu} &= \frac{1}{N} \sum_{a=1}^N 2 \left[f_c - f_{(a)} + \Delta x_{(a)}^\nu G_\nu + \frac{1}{2} \Delta x_{(a)}^\nu \Delta x_{(a)}^\lambda G_{\nu\lambda} \right] \nabla x_{(a)}^\mu \\ &= -2 \cdot \frac{1}{N} \sum_{a=1}^N f_{(a)} \Delta x_{(a)}^\mu + 2 R^{\mu\nu} G_\nu + R^{\mu\nu\lambda} G_{\nu\lambda} \end{aligned} \quad (A10)$$

1086 where the 3 order tensor $R^{\mu\nu\lambda}$ is defined as

$$R^{\mu\nu\lambda} \equiv \frac{1}{N} \sum_{a=1}^N \Delta x_{(a)}^{\mu} \Delta x_{(a)}^{\nu} \Delta x_{(a)}^{\lambda}. \quad (A11)$$

From Equation (A10) we get

$$R^{\mu\nu} G_{\nu} = \frac{1}{N} \sum_a \left(x_{(a)}^{\mu} - x_c^{\mu} \right) f_a - \frac{1}{2} R^{\mu\nu\lambda} G_{\nu\lambda}. \quad (A12)$$

Thus the linear gradients at the central point are

$$G_{\nu} = (\nabla_{\nu} f)_c = \left(R^{-1} \right)_{\nu\mu} \cdot \frac{1}{N} \sum_a \left(x_{(a)}^{\mu} - x_c^{\mu} \right) f_a - \frac{1}{2} \left(R^{-1} \right)_{\nu\mu} R^{\mu\sigma\lambda} G_{\sigma\lambda}. \quad (A13)$$

Here R^{-1} satisfies $\left(R^{-1} \right)_{\nu\sigma} R^{\sigma\lambda} = R^{\lambda\sigma} \left(R^{-1} \right)_{\sigma\nu} = \delta_{\nu}^{\lambda}$. These are the first order gradients of the physical quantity in space and time at the central point.

Under the linear approximation, the quadratic gradient is neglected, i.e., $G_{\nu\lambda} = 0$.

From the formula (A8'), the physical quantity at the central point is

$$f_0 = \frac{1}{N} \sum_a f_{(a)}. \quad (A14)$$

From the formula (A13), the first order gradients of the physical quantity in space and time are

$$G_{\nu} = (\nabla_{\nu} f)_c = \left(R^{-1} \right)_{\nu\mu} \cdot \frac{1}{N} \sum_a \left(x_{(a)}^{\mu} - x_c^{\mu} \right) f_a. \quad (A15)$$

Appendix B: Natures of the magnetic rotation tensor

In previous investigations [Shen et al., 2007; Shen et al., 2008a, b], the MRA (magnetic rotation analysis) method has been put forward to study the 3 dimensional rotational properties of the magnetic field. We may construct the magnetic rotational tensor \mathbf{S} based on the gradient of the magnetic unit vector $\hat{\mathbf{b}}$, which is defined as

1107 $S_{ij} \equiv \nabla_i b_l \nabla_j b_l$. Because the tensor \mathbf{S} is symmetrical ($S_{ij} = S_{ji}$, $i, j = 1, 2, 3$), it has
 1108 three eigenvectors, $\hat{\mathbf{X}}_1$, $\hat{\mathbf{X}}_2$ and $\hat{\mathbf{X}}_3$, and three corresponding eigenvalues, μ_1 , μ_2
 1109 and μ_3 with $\mu_1 \geq \mu_2 \geq \mu_3 \geq 0$. Actually, the third eigenvalue μ_3 is zero. Fadanelli,
 1110 et al. (2019) has presented one verification on this property of the magnetic rotational
 1111 tensor. To facilitate the understanding, here we can show another verification as the
 1112 following.

1113 The length of $\hat{\mathbf{b}}$ is 1, and $\hat{\mathbf{b}} \cdot \hat{\mathbf{b}} = 1$, so that

$$1114 \quad \nabla_i (\hat{\mathbf{b}} \cdot \hat{\mathbf{b}}) = (\nabla_i b_j) b_j = 0. \quad (\text{B1})$$

1115 To ensure the existence of $\hat{\mathbf{b}}$, it is necessary that

$$1116 \quad \text{Det}(\nabla_i b_j) = 0. \quad (\text{B2})$$

1117 Based on its definition, the determinant of the magnetic rotation tensor is

$$1118 \quad \text{Det}(S_{ij}) = \text{Det}(\nabla_i b_l) \cdot \text{Det}(\nabla_j b_l) = 0. \quad (\text{B3})$$

1119 On the other hand,

$$1120 \quad \text{Det}(S_{ij}) = \mu_1 \mu_2 \mu_3, \quad \mu_1 \geq \mu_2 \geq \mu_3 \geq 0. \quad (\text{B4})$$

1121 Thus equations (A3) and (A4) reduce to

$$1122 \quad \mu_3 = 0. \quad (\text{B5})$$

1123 So that the third eigenvalue μ_3 of the magnetic rotation tensor $S_{ij} = \nabla_i b_l \nabla_j b_l$ is null
 1124 definitely.

1125

1126

1127 **Appendix C: Another verification on the formula of torsion of MFLs in terms**
 1128 **of magnetic gradients**

1129

1130 Based on the definition, the torsion of the MFLs

$$\begin{aligned}
 \tau &= \frac{1}{\kappa} \frac{d\boldsymbol{\kappa}}{ds} \cdot \hat{\mathbf{N}} \\
 &= \frac{1}{\kappa} \frac{d}{ds} \left(\frac{d\mathbf{B}}{ds} \right) \cdot \hat{\mathbf{N}} \\
 &= \frac{1}{\kappa} \frac{d}{ds} \left(\frac{1}{B} \frac{d\mathbf{B}}{ds} + \mathbf{B} \frac{d}{ds} \frac{1}{B} \right) \cdot \hat{\mathbf{N}} \\
 &= \frac{1}{\kappa} \left(\frac{1}{B} \frac{d^2 \mathbf{B}}{ds^2} + 2 \frac{d}{ds} \frac{1}{B} \cdot \frac{d\mathbf{B}}{ds} + \mathbf{B} \frac{d^2}{ds^2} \frac{1}{B} \right) \cdot \hat{\mathbf{N}}. \tag{C1}
 \end{aligned}$$

1133 Due to $\mathbf{B} \cdot \hat{\mathbf{N}} = B \hat{\mathbf{b}} \cdot \hat{\mathbf{N}} = 0$, $\frac{d\mathbf{B}}{ds} \cdot \hat{\mathbf{N}} = \left(B \frac{d\hat{\mathbf{b}}}{ds} + \frac{dB}{ds} \hat{\mathbf{b}} \right) \cdot \hat{\mathbf{N}} = \left(B \boldsymbol{\kappa} + \frac{dB}{ds} \hat{\mathbf{b}} \right) \cdot \hat{\mathbf{N}} = 0$, the

1134 second and third terms at the left hand of the above formula disappear. Therefore

$$\tau = \frac{1}{\kappa B} \frac{d^2 \mathbf{B}}{ds^2} \cdot \hat{\mathbf{N}}. \tag{C2}$$

1136 This gives the relationship between the torsion of the MFLs and the second order

1137 derivative of the magnetic field along the MFLs.

1138 Furthermore, the torsion of the MFLs becomes

$$\begin{aligned}
 \tau &= \frac{1}{\kappa B} \hat{\mathbf{N}} \cdot \frac{d}{ds} \left(\frac{1}{B} B_i \partial_i \mathbf{B} \right) \\
 &= \frac{1}{\kappa B} \hat{\mathbf{N}} \cdot \left[\left(\frac{d}{ds} \frac{1}{B} \right) B_i \partial_i \mathbf{B} + \frac{1}{B} \left(\frac{d}{ds} B_i \right) \partial_i \mathbf{B} + \frac{1}{B} B_i \frac{d}{ds} \partial_i \mathbf{B} \right]. \tag{C3}
 \end{aligned}$$

1141 The first term at the left hand of the above formula disappear because

1142 $\hat{\mathbf{N}} \cdot (B_i \partial_i \mathbf{B}) = B \hat{\mathbf{N}} \cdot \frac{d}{ds} \mathbf{B} = -B \cdot \frac{d\hat{\mathbf{N}}}{ds} \cdot \mathbf{B} = -B (-\tau \hat{\mathbf{K}}) \cdot \mathbf{B} = 0$. So that the torsion is

$$\begin{aligned}
 \tau &= \frac{1}{\kappa B} \hat{\mathbf{N}} \cdot \left[\frac{1}{B} \left(\frac{d}{ds} B_i \right) \partial_i \mathbf{B} + \frac{1}{B} B_i \frac{d}{ds} \partial_i \mathbf{B} \right] \\
 &= \frac{1}{\kappa B^3} N_m B_n \partial_n B_i \partial_i B_m + \frac{1}{\kappa B^3} N_m B_i B_n \partial_n \partial_i B_m. \tag{C4}
 \end{aligned}$$

1145

1146

1147 **Appendix D: Geometry of the MFLs in 1 dimensional current sheets**

1148

1149 It is assumed that the magnetic field in the 1 dimensional currents is

1150 $\mathbf{B} = B_x \hat{\mathbf{e}}_x + B_y \hat{\mathbf{e}}_y + B_z \hat{\mathbf{e}}_z$. Let the z axis to be along the normal to the 1 dimensional

1151 current sheets. The components of the magnetic field in the x and y directions are

1152 invariants, i.e., $\partial x = 0$, $\partial y = 0$. Therefore the components of the magnetic field in the

1153 Cartesian coordinates are

$$1154 \quad \begin{cases} B_x = B_0 \eta(z) \\ B_y = \text{Const.} \\ B_z = \text{Const.} \end{cases} \quad (\text{D1})$$

1155 We may choose that $B_z \geq 0$, $B_0 > 0$, $\partial_z B_x = B_0 \eta'(z) > 0$. As for the Harris

1156 current sheets [Harris, 1962], $\eta(z) = \tanh(z/h)$, where h is the half width of the

1157 current sheets. The total magnetic strength is $B = (B_x^2 + B_y^2 + B_z^2)^{1/2}$.

1158 The curvature of the MFLs is

$$\begin{aligned} \kappa &= \hat{\mathbf{b}} \cdot \nabla \hat{\mathbf{b}} \\ &= B^{-2} (\mathbf{B} \cdot \nabla) \mathbf{B} - \frac{1}{2} B^{-4} (\mathbf{B} \cdot \nabla) B^2 \cdot \mathbf{B} \\ &= B^{-2} B_z \partial_z \mathbf{B} - \frac{1}{2} B^{-4} B_z \partial_z B_x^2 \cdot \mathbf{B} \\ &= B^{-2} B_z \partial_z B_x \hat{\mathbf{e}}_x - B^{-4} B_z B_x \partial_z B_x \cdot \mathbf{B} \\ &= B^{-4} B_z \partial_z B_x \cdot (B^2 \hat{\mathbf{e}}_x - B_x \mathbf{B}) \\ &= B^{-4} B_z \partial_z B_x \left[(B_y^2 + B_z^2) \hat{\mathbf{e}}_x - B_x B_y \hat{\mathbf{e}}_y - B_x B_z \hat{\mathbf{e}}_z \right] \end{aligned}$$

(D2)

1161 The value of the curvature is

$$\kappa = B^{-4} B_z \partial_z B_x \cdot B (B_y^2 + B_z^2)^{1/2} = B^{-3} B_z (B_y^2 + B_z^2)^{1/2} \partial_z B_x . \quad (D3)$$

The radius of the curvature is $R_c = 1 / \kappa$.

The principal normal vector is

$$\hat{\mathbf{K}} = \boldsymbol{\kappa} / \kappa = B^{-1} (B_y^2 + B_z^2)^{1/2} \left[(B_y^2 + B_z^2) \hat{\mathbf{e}}_x - B_x B_y \hat{\mathbf{e}}_y - B_x B_z \hat{\mathbf{e}}_z \right] . \quad (D4)$$

The binormal vector is

$$\begin{aligned} \hat{\mathbf{N}} &= \hat{\mathbf{b}} \times \hat{\mathbf{K}} \\ &= B^{-1} \mathbf{B} \times \hat{\mathbf{K}} \\ &= B^{-2} (B_y^2 + B_z^2)^{1/2} (B_x \hat{\mathbf{e}}_x + B_y \hat{\mathbf{e}}_y + B_z \hat{\mathbf{e}}_z) \times \left[(B_y^2 + B_z^2) \hat{\mathbf{e}}_x - B_x B_y \hat{\mathbf{e}}_y - B_x B_z \hat{\mathbf{e}}_z \right] \\ &= B^{-2} (B_y^2 + B_z^2)^{1/2} (\hat{\mathbf{e}}_y B_z B^2 - \hat{\mathbf{e}}_z B_y B^2) \\ &= (B_y^2 + B_z^2)^{1/2} (B_z \hat{\mathbf{e}}_y - B_y \hat{\mathbf{e}}_z) \end{aligned} \quad (D5)$$

Therefore, the binormal of the MFLs is constant. Then, based on the definition (58),

the torsion of MFLs is

$$\tau = -\frac{1}{\kappa} \boldsymbol{\kappa} \cdot \frac{d\hat{\mathbf{N}}}{ds} = 0 . \quad (D6)$$

So that, the MFLs in the current sheets as formulated by (D1) are plane curves.

For the asymmetric current sheet, $\eta(z) = \alpha + \tanh(z/h)$, $1 > \alpha > 0$. As for the shock

fronts, $B_y = 0$, and $\eta(z) = \alpha + \tanh(z/h)$, $\alpha > 1$. For these cases, the MFLs are

plane curves with zero torsion.

However, as shown in actual observations, the component B_y is not constant,

which maximises at the center of neutral sheets and is decreasing away from the

center of the current sheets [Rong, et al., 2012]. The MFLs in the magnetotail current

sheets often have a shape of helix in the neutral sheets (Shen, et al., 2008a).

Appendix E: Geometry of Cylindrical helical MFLs in magnetic flux ropes with axial symmetry

Cylindrical spiral MFLs are common in space plasmas, as seen in FTEs [Russell and Elphic, 1979; Lee et al., 1985; Liu and Hu, 1988; Lockwood and Hapgood, 1998; Wang et al., 2007; Liu et al., 2018] or flux ropes caused by local magnetic reconnection processes [Sibeck, et al., 1984; Slavin et al., 1989; Kivelson et al., 1995; Slavin et al., 2003; Zong et al., 2004; Pu et al., 2005; Zhang et al., 2007], fast tailward escaping plamoids [Slavin et al., 1989; Slavin et al., 1995], etc.

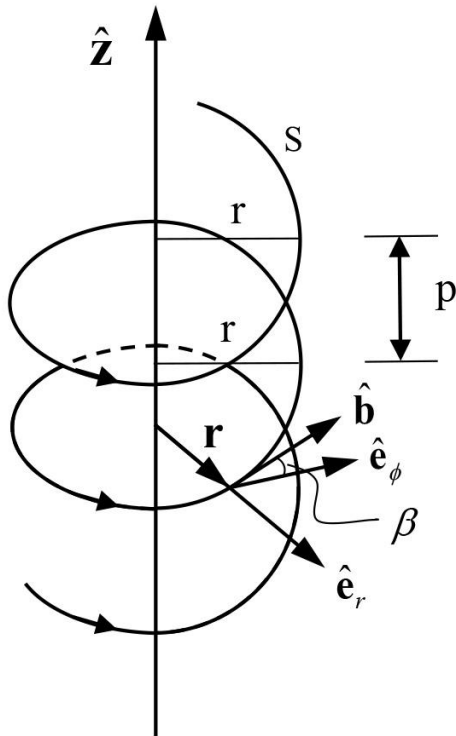


Figure E1 Demonstration on the cylindrical spiral MFLs.

As shown in Figure E1, polar coordinates are used. The central axis is along the z axis, the arc length is s, the distance from the central axis is r, and the azimuthal angle is ϕ . The radial unit vector is $\hat{\mathbf{e}}_r$, and the azimuthal unit vector is $\hat{\mathbf{e}}_\phi$. The tangent vector of the MFLs is

$$\hat{\mathbf{b}} = \mathbf{B} / B = \cos \beta \hat{\mathbf{e}}_\phi + \sin \beta \hat{\mathbf{e}}_z, \quad (\text{E1})$$

where β is the helix angle of the MFLs. The helical pitch is $p = 2\pi r \tan \beta$. Define the rotation frequency $\omega \equiv d\phi / ds$. Then $\omega = \phi / s = 2\pi / (p / \sin \beta) = \cos \beta / r$. Thus,

$$\frac{ds}{d\phi} = \frac{1}{\omega} = \frac{r}{\cos \beta}. \quad (\text{E2})$$

The curvature of the MFLs is

$$\kappa = \frac{d\hat{\mathbf{b}}}{ds} = \frac{d\phi}{ds} \frac{d\hat{\mathbf{b}}}{d\phi} = \omega \cos \beta \frac{d\hat{\mathbf{e}}_\phi}{d\phi} = -\omega \cos \beta \hat{\mathbf{e}}_r. \quad (\text{E3})$$

Where, $\frac{d}{d\phi} \hat{\mathbf{e}}_\phi = -\hat{\mathbf{e}}_r$ is used. So that the curvature is

$$\kappa = -\omega \cos \beta \hat{\mathbf{e}}_r. \quad (\text{E3}')$$

The value of the curvature is

$$\kappa = \omega \cos \beta = r \omega^2 = r^{-1} \cos^2 \beta. \quad (\text{E4})$$

The radius of curvature is

$$R_c = r (\cos \beta)^{-2}. \quad (\text{E5})$$

The principal vector of the helical MFLs is $\hat{\mathbf{K}} = \kappa / \kappa = -\hat{\mathbf{e}}_r$, that is along the radial direction. The binormal $\hat{\mathbf{N}}$ is

$$\hat{\mathbf{N}} = \hat{\mathbf{b}} \times \hat{\mathbf{K}} = (\cos \beta \hat{\mathbf{e}}_\phi + \sin \beta \hat{\mathbf{e}}_z) \times (-\hat{\mathbf{e}}_r) = \cos \beta \cdot \hat{\mathbf{e}}_z - \sin \beta \cdot \hat{\mathbf{e}}_\phi. \quad (\text{E6})$$

The variation rate of the binormal $\hat{\mathbf{N}}$ along the MFLs is

$$\frac{d\hat{\mathbf{N}}}{ds} = \frac{d\phi}{ds} \cdot \frac{d\hat{\mathbf{N}}}{d\phi} = \omega(-\sin\beta) \frac{d\hat{\mathbf{e}}_\phi}{d\phi} = \omega \sin\beta \cdot \hat{\mathbf{e}}_r. \quad (\text{E7})$$

So that the torsion of the helical MFLs is

$$\tau = -\hat{\mathbf{K}} \cdot \frac{d\hat{\mathbf{N}}}{ds} = \hat{\mathbf{e}}_r \cdot \omega \sin\beta \hat{\mathbf{e}}_r = \omega \sin\beta = r^{-1} \sin\beta \cos\beta = 2\pi p^{-1} \sin^2\beta \quad (\text{E8})$$

On the contrary, if the curvature κ and torsion τ of the cylindrical spiral MFLs have been measured, the helix angle, the distance from the central axis, the spiral pitch and the rotation frequency can be expressed as

$$\tan\beta = \frac{\tau}{\kappa} = \tau R_c, \quad (\text{E9})$$

$$r = \kappa^{-1} \cos^2\beta = \frac{\kappa}{\tau^2 + \kappa^2}, \quad (\text{E10})$$

$$p = 2\pi r \tan\beta = \frac{2\pi\tau}{\tau^2 + \kappa^2}, \quad (\text{E11})$$

$$\omega = \frac{\cos\beta}{r} = \sqrt{\tau^2 + \kappa^2}. \quad (\text{E12})$$

Any arbitrary magnetic field line can locally be fitted by a cylindrical spiral arc with the same curvature and torsion. The curvatures of the magnetic field lines are always non-negative. However, the torsion of one MFL can be either positive or negative. When $\tau > 0$, the helix angle $\beta > 0$, the magnetic field line is locally a right-hand cylindrical spiral; while $\tau < 0$, $\beta < 0$, it is a left-hand one.

1236

1237 **References**

1238 Angelopoulos, V. (2008). The THEMIS mission. *Space Science Reviews*, 141(1 - 4),
1239 5 - 34. <https://doi.org/10.1007/s11214-008-9336-1>.

1240 Balogh, A., et al. (2001), The Cluster magnetic field investigation: overview of
1241 inflight performance and initial results, *Ann. Geophys.*, 19, 1207.

1242 Burch, J. L., Moore, T. E., Torbert, R. B., & Giles, B. L. (2016). Magnetospheric
1243 Multiscale overview and science objectives. *Space Science Reviews*, 199(1 - 4),
1244 5 - 21. <https://doi.org/10.1007/s11214-015-0164-9>.

1245 Chanteur, G. (1998), Spatial Interpolation for four spacecraft: Theory, in *Analysis*
1246 *Methods for Multi-Spacecraft Data*, edited by G. Paschmann and P. W. Daly, p. 349,
1247 ESA Publ. Div., Noordwijk, Netherlands.

1248 De Keyser, J., Dunlop, M. W., Darrouzet, F., and D'ecr'eu, P. M. E.: Least-squares
1249 gradient calculation from multi-point observations of scalar and vector fields:
1250 Methodology and applications with Cluster in the plasmasphere, *Ann. Geophys.*,
1251 25, 971–987, 2007, <http://www.ann-geophys.net/25/971/2007/>.

1252 Dunlop, M. W., and T. I. Woodward (1998), Multi-spacecraft discontinuity analysis:
1253 Orientation and motion, in *Analysis Methods for Multi-Spacecraft Data*, edited by
1254 G. Paschmann and P. W. Daly, p. 271, ESA Publications Division, Noordwijk, The
1255 Netherlands.

1256 Dunlop, M. W., D. J. Southwood, K.-H. Glassmeier, and F. M. Neubauer, Analysis of
1257 multipoint magnetometer data, *Adv. Space Res.*, 8, 273, 1988.

Dunlop, M. W., Y.-Y. Yang, J.-Y. Yang, H. Luhr, C. Shen, N. Olsen, Q. -H. Zhang, Y.V. Bogdanova, J.-B. Cao, P. Ritter, K. Kauristie, A. Masson and R. Haagmans (2015), Multi-spacecraft current estimates at Swarm, *J. Geophys. Res.*, 120, doi:10.1002/2015JA021707.

Dunlop, M W, Haaland, S., Escoubet, P. And X-C Dong (2016), Commentary on accessing 3-D currents in space: Experiences from Cluster, *J. Geophys. Res.*, 121, doi:10.1002/2016JA022668.

Dunlop, M. W., S. Haaland, X-C. Dong, H. Middleton, P. Escoubet, Y-Y. Yang, Q-H Zhang, J-K. Shi and C.T. Russell (2018), Multi-point analysis of current structures and applications: Curlometer technique, in *Electric Currents in Geospace and Beyond* (eds A. Keiling, O. Marghitu, and M. Wheatland), John Wiley & Sons, Inc, Hoboken, N.J., AGU books, doi: 10.1002/9781119324522.ch4

Dunlop, M. W. J.-Y. Yang, Y-Y. Yang, H. Lühr and J.-B. Cao (2020), Multi-spacecraft current estimates at Swarm, in *Multi-satellite data analysis*, edited by M W Dunlop and H Luehr, *ISSI scientific reports volume 17*, Springer, DOI:10.1007/978-3-030-26732-2_5.

Eastwood, J. P., T. D. Phan, P. A. Cassak et al. (2016), Ion-scale secondary flux ropes generated by magnetopause reconnection as resolved by MMS, *Geophys. Res. Lett.*, 43, 4716–4724, doi:10.1002/2016GL068747.

Escoubet, C. P., Fehringer, M., & Goldstein, M. (2001), Introduction: The Cluster mission, *Annales Geophysicae*, 19, 1197-1200, <https://doi.org/10.5194/angeo-19-197-2001>.

Fadanelli, S., B. Lavraud, F. Califano, et al. (2019). Four - spacecraft measurements of the shape and dimensionality of magnetic structures in the near - Earth plasma environment. *Journal of Geophysical Research: Space Physics*, 124. <https://doi.org/10.1029/2019JA026747>

1284 Friis-Christensen, E., H. Lühr, and G. Hulot (2006), Swarm: A constellation to study
1285 the Earth's magnetic field, *Earth Planets Space*, 58, 351–358.

1286 Hamrin, M. , K. Rönmark, N. Börnin, J. Vedin, and A. Vaivads (2008), Gals - gradient
1287 analysis by least squares, *Annales Geophysicae*, 26(11), 3491-3499.

1288 Harris, E. G. (1962), On a plasma sheath separating regions of oppositely directed
1289 magnetic field, *Nuovo Cimento XXIII*, 115.

1290 Harvey, C. C. (1998), Spatial gradients and the volumetric tensor, in *Analysis Methods*
1291 *for Multi-Spacecraft Data*, edited by G. Paschmann and P. W. Daly, p. 307, ESA
1292 Publications Division, Noordwijk, The Netherlands.

1293 Kivelson, M. G., K. K. Khurana, R. J. Walker, L. Kepko, and D. Xu (1995), Flux
1294 ropes, interhemispheric conjugacy, and magnetospheric current closure, *J.*
1295 *Geophys. Res.*, 10(A12), 27,341–27,350, doi:10.1029/96JA02220.

1296 Lavraud, B., Zhang, Y. C., Vernisse, Y., Gershman, D. J., Dorelli, J., Cassak, P. A., et al.
1297 (2016). Currents and associated electron scattering and bouncing near the diffusion
1298 region at Earth's magnetopause. *Geophysical Research Letters*, 43, 6036–6043.
1299 <https://doi.org/10.1002/2016GL068359>.

1300 Lee, L. C., Z. F. Fu, and S.-I. Akasofu (1985), A simulation study of forced
1301 reconnection processes and magnetospheric storms and substorms, *J. Geophys.*
1302 *Res.*, 90(A11), 896–910, doi:10.1029/JA090iA11p10896.

1303 Liu, Y. Y., et al. (2019), SOTE: A nonlinear method for magnetic topology
1304 reconstruction in space plasmas, *The Astrophysical Journal Supplement Series*
1305 244.31.

1306 Liu, Z.-X., C. P. Escoubet, Z. Pu, H. Laakso, J. Q. Shi, C. Shen, M. Hapgood,
 1307 (2005), The Double Star Mission, *Ann Geophysicae*, 23, 2707-2712, doi:
 1308 10.5194/angeo-23-2707-2005.

1309 Liu, Z. X., and Y. D. Hu (1988), Local magnetic reconnection caused by vortices in the
 1310 flow field, *Geophys. Res. Lett.*, **12**, 752.

1311 Liu, Y., Z. Y. Pu, et al. (2018), Ion-scale structures in flux ropes observed by MMS at
 1312 the magnetopause (in Chinese), *Chin. J. Space Sci.*, 38(2), 147-168.
 1313 DOI:10.11728/cjss2018.02.147.

1314 Lockwood, M., and M. A. Hapgood (1998), On the cause of a magnetospheric flux
 1315 transfer event, *J. Geophys. Res.*, 103(A11), 26,453–26,478,
 1316 doi:10.1029/98JA02244.

1317 McComas, C., T. Russell, R. C. Elphic, and S. J. Bame, The near-Earth cross-tail
 1318 current sheet: Detailed ISEE 1 and 2 case studies, *J. Geophys. Res.*, 91, 4287,
 1319 1986.

1320 Ogilvie, K. W., T. Von Rosenvinge, and A. C. Durney (1977), International
 1321 Sun-Earth explorer: A three-spacecraft program, *Science*, 198, 131–138.

1322 Pu, Z.Y., Q.-G. Zong, T.A. Fritz, C.J. Xiao, Z.Y. Huang, S.Y. Fu, Q.Q. Shi, M.W.
 1323 Dunlop, K.-H. Glassmeier, A. Balogh, P. Daly, H. Reme, J. Dandouras, J.B. Cao,
 1324 Z.X. Liu, C. Shen, and J.K. Shi (2005), Multiple flux rope events at the
 1325 high-latitude magnetopause: cluster/rapid observation on 26 January, 2001, *Surv.*
 1326 *Geophys.* **26**(1–3), 193–214, <https://doi.org/10.1007/s10712-005-1878-0>

1327 Rong, Z. J., W. X. Wan, C. Shen, X. Li, M. W. Dunlop, A. A. Petrukovich, T. L.

Zhang, and E. Lucek (2011), Statistical survey on the magnetic structure in magnetotail current sheets, *J. Geophys. Res.*, 116, A09218, doi:10.1029/2011JA016489.

Rong, Z. J., W. X. Wan, C. Shen, X. Li, M. W. Dunlop, A. A. Petrukovich, L.-N. Hau, E. Lucek, H. Rème (2012), Profile of strong magnetic field By component in magnetotail current sheets, *J. Geophys. Res.*, 117, A06216, doi:10.1029/2011JA017402.

Russell, C. T., Anderson, B. J., Baumjohann, W., Bromund, K. R., Dearborn, D., Fischer, D., et al. (2016), The Magnetospheric Multiscale magnetometers, *Space Science Reviews*, 199(1-4), 189-256, <https://doi.org/10.1007/s11214-014-0057-3>.

Russell, C. T., and R. C. Elphic (1979), ISEE observations of flux transfer events at the dayside magnetopause, *Geophys. Res. Lett.*, 6(1), 33–36, doi:10.1029/GL006i001p00033.

Shen, C., X. Li, M. Dunlop, Z. X. Liu, A. Balogh, D. N. Baker, M. Hapgood, and X. Wang (2003), Analyses on the geometrical structure of magnetic field in the current sheet based on cluster measurements, *J. Geophys. Res.*, 108(A5), 1168, doi:10.1029/2002JA009612.

Shen, C., and Z. -X. Liu (2005), Double Star Project Master Science Operations Plan, *Ann. Geophysicae*, 23, 2851-2859, doi: 10.5194/angeo-23-2851-2005. Shen, C., X. Li, M. Dunlop, Q. Q. Shi, Z. X. Liu, E. Lucek, and Z. Q. Chen (2007), Magnetic

1349 field rotation analysis and the applications, *J. Geophys. Res.*, 112, A06211,
 1350 doi:10.1029/2005JA011584.

1351 Shen, C., Z. Liu, X. Li, M. W. Dunlop, E. A. Lucek, Z. Rong, Z. Chen, C. P. Escoubet,
 1352 H. V. Malova, A. T. Y. Lui, A. N. Fazakerley, A. P. Walsh, and C. Mouikis
 1353 (2008a), Flattened Current Sheet and its Evolution in Substorms, *J. Geophys. Res.*,
 1354 113, A07S21, doi:10.1029/2007JA012812.

1355 Shen, C., Z. J. Rong, X. Li, Z. X. Liu, M. Dunlop, E. Lucek, H.V. Malova (2008b),
 1356 Magnetic Configurations of Tail Tilted Current Sheets, *Ann. Geophys.*, 26,
 1357 3525–3543.

1358 Shen, C., et al. (2011), The magnetic configuration of the high-latitude cusp and
 1359 dayside magnetopause under strong magnetic shears, *J. Geophys. Res.*, 116,
 1360 A09228, doi:10.1029/2011JA016501.

1361 Shen, C., et al. (2012a), Spatial gradients from irregular, multiple-point spacecraft
 1362 configurations, *J. Geophys. Res.*, 117, A11207, doi:10.1029/2012JA018075.

1363 Shen, C., Z. J. Rong, and M. Dunlop (2012b), Determining the full magnetic field
 1364 gradient from two spacecraft measurements under special constraints, *J. Geophys.*
 1365 *Res.*, 117, A10217, doi:10.1029/2012JA018063.

1366 Shen, C., et al. (2014), Direct calculation of the ring current distribution and magnetic
 1367 structure seen by Cluster during geomagnetic storms, *J. Geophys. Res.*
 1368 *SpacePhysics*, 119, doi:10.1002/2013JA019460.

1369 Shi, Q. Q., Shen, C., Dunlop, M. W., Pu, Z. Y., Zong, Q.-G., Liu, Z. X., Lucek, E., and
 1370 Balogh, A., 2006, Motion of observed structures calculated from multi-point

1371 magnetic field measurements: Application to Cluster, Geophys. Res. Lett., 33,
 1372 L08109, doi:10.1029/2005GL025073.

1373 Sibeck, D. G., G. L. Siscoe, J. A. Slavin, E. J. Smith, S. J. Bame, and F. L. Scarf
 1374 (1984), Magnetotail flux ropes, Geophys. Res. Lett., 11(10), 1090–1093,
 1375 doi:10.1029/GL011i010p01090.

1376 Slavin, J. A., et al. (1989), CDAW 8 observations of plasmoid signatures in the
 1377 geomagnetic tail: An assessment, J. Geophys. Res., 94(A11), 15,153–15,175,
 1378 doi:10.1029/JA094iA11p15153.

1379 Slavin, J. A., C. J. Owen, and M. M. Kuznetsova (1995), ISEE3 observations of
 1380 plasmoids with flux rope magnetic topologies, Geophys. Res. Lett., 22(15),
 1381 2061–2064, doi:10.1029/95GL01977.

1382 Slavin, J. A., et al. (2003), Cluster electric current density measurements within a
 1383 magnetic flux rope in the plasma sheet, Geophys. Res. Lett., 30(7), 1362,
 1384 doi:10.1029/2002GL016411.

1385 Song, P., and C. T. Russell (1999), Time series data analyses in space physics, *Space*
 1386 *ence Reviews*, 87(3-4), 387-463.

1387 Torbert, R. B., Vaith, H., Granoff, M., Widholm, M., Gaidos, J. A., Briggs, B. H., et al.
 1388 (2015). The electron drift instrument for MMS. *Space Science Reviews*, 199(1 - 4),
 1389 283 - 305. <https://doi.org/10.1007/s11214-015-0182-7>

1390 Torbert, R. B., Dors, I., Argall, M. R., Genestreti, K. J., Burch, J. L., Farrugia, C. J., et
 1391 al. (2020). A new method of 3 - D magnetic field reconstruction. *Geophysical*
 1392 *Research Letters*, 47, e2019GL085542. <https://doi.org/10.1029/2019GL085542>.

1393 Vogt, J., G. Paschmann, and G. Chanteur (2008), Reciprocal Vectors, in
 1394 Multi-Spacecraft Analysis Methods Revisited, ISSI Sci. Rep., SR-008, edited by G.
 1395 Paschmann and P. W. Daly, pp. 33–46, Kluwer Academic Pub., Dordrecht,
 1396 Netherlands.

1397 Vogt, J., A. Albert, and O. Marghitu (2009), Analysis of three-spacecraft data using
 1398 planar reciprocal vectors: Methodological framework and spatial gradient
 1399 estimation, *Ann. Geophys.*, 27, 3249–3273, doi:10.5194/angeo-27-3249-2009.

1400 Wang J., M. W. Dunlop, Z.Y. Pu, et al. (2007), TC1 and Cluster observation of an
 1401 FTE on 4 January 2005: A close conjunction, *Geophys. Res. Lett.*, 34, L03106,
 1402 doi:10.1029/2006GL028241.

1403 Xiao, C., W. Liu, C. Shen, H. Zhang, & Z. Rong (2018). Study on the curvature and
 1404 gradient of the magnetic field in Earth's cusp region based on the magnetic
 1405 curvature analysis method. *Journal of Geophysical Research: Space Physics*, 123,
 1406 3794–3805. <https://doi.org/10.1029/2017JA025028>

1407 Zhang, C., Rong, Z. J., Shen, C., Klinger. L., Gao. J. W., Slavin. J. A., Zhang, Y. C.,
 1408 Cui. J., Wei. Y., (2020). Examining the magnetic geometry of magnetic flux ropes
 1409 from the view of single-point analysis. *The Astrophysical Journal.*, doi:
 1410 10.3847/1538-4357/abba16

1411 Zhang, Y. C., Z. X. Liu, C. Shen, A. Fazakerley, M. Dunlop, H. Reme, E. Lucek, A. P.
 1412 Walsh, and L. Yao (2007). The magnetic structure of an earthward-moving flux
 1413 rope observed by Cluster in the near-tail, *Ann. Geophys.*, 25, 1471-1476.

1414 Zong, Q. G., et al. (2004), Cluster observations of earthward flowing plasmoid in the

